

We thank the reviewer for the useful suggestions to improve the paper. These comments are all valuable and very helpful for revising and improving our manuscript, as well as the important guiding significance to our research. These changes in the revised manuscript have been marked in the track changes version manuscript, as well as the point-to-point responses have been listed as follows:

## **Response to reviewer #2**

**Comment:** This manuscript describes the use of multistatic meteor radars to study the mesosphere and lower thermosphere using installations in central China to illustrate their methods. It follows the structure of other similar papers and does not bring new content to the field other than a new location. (It was much less clear than its predecessors with missing variable definitions and undescribed terms.) As such, it does not warrant publication in AMT.

**Response:** Thank you for your great suggestion. We agree with the shortcomings of our study, especially the innovation of methods/algorithms and a few days of observation. To provide more new information based on the bistatic meteor radar system, we extended the observation data to more than 1 year and added a new section in the revised manuscript. This study will provide the first investigation of the seasonal variations in MLT dynamics at lower-midlatitudes (near 30°N) in the Northern Hemisphere.

*Here is what we have added in the revised manuscript.*

### **5. Seasonal variation dynamics parameters in the MLT region**

This section uses the methodology described in the previous section to estimate the seasonal variation in MLT dynamics parameters, including horizontal wind deformations and gravity wave (GW) momentum fluxes, in the MLT region in the middle latitudes of the Northern Hemisphere from February 2022 to February 2023. As shown in Figure 13, we present the seasonal variations in monthly mean horizontal winds, horizontal divergence, relative vorticity, stretching deformation, and shearing deformation. In Figure 13a, the zonal component shows westward winds in spring

(March, April and May) and eastward winds in summer, autumn and winter (May to February) below 84 km, which is the characteristic of annual variation. However, within 84 to 90 km, the zonal wind shows maxima value in summer and winter as well as minimum value at the spring and autumn equinox, suggesting semiannual variation. From 90 to 96 km, the zonal wind again shows annual variation, with large eastward winds in spring to summer and low westward winds in autumn to winter. The overall zonal wind between 80 and 96 km is characterized by annual variation. During spring to summer, the zonal wind increases (greater eastward and lesser westward) with altitude, reaching a peak value of approximately 50 m/s at 96 km in May. In autumn and winter, the zonal wind decreases (lesser eastward and greater westward) with altitude, reaching a minimum value at 96 km in November.

In Figure 13b, the meridional winds show similar structures to the zonal winds. Below 86 km, the meridional wind is southward in spring to summer and northward in autumn to winter. Meanwhile, at latitudes between 88 and 96 km, the meridional wind is northward in spring to summer and is northward in autumn to winter, and the maximum values of northward and southward winds are 20 m/s and 15 m/s in May and October, respectively.

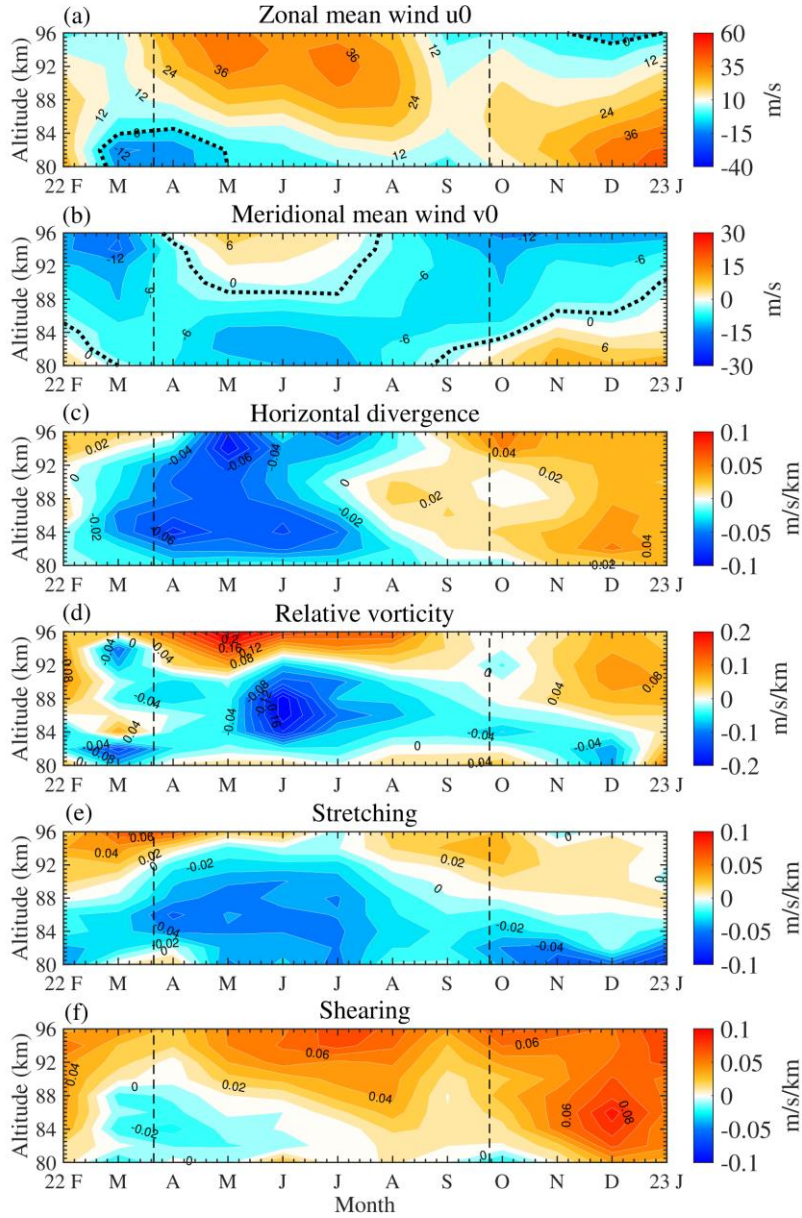


**Figure 13.** The seasonal values of horizontal winds and wind deformations from February 1, 2022 to February 1, 2023 at altitudes ranging from 80 to 96 km: (a) mean zonal wind, (b) mean meridional wind, (c) horizontal divergence, (d) relative vorticity, (e) stretching deformation, and (f) shearing deformation.

In Figures 13c and 13d, the horizontal divergence and stretching deformation are calculated by the gradient terms  $u_x$  and  $v_y$ , and they portray a similar seasonal variation. The divergence is almost negative below 84 km. Within 84 to 96 km, the value is still negative in March to June, reaching -0.1 m/s/km at 96 km in May. In the remaining months of the year, the divergence is positive, reaching 0.08 m/s/km at 94 km in November. The maximum values of divergence (convergence) correspond to the

maxima of eastward/northward (westward/southward) wind velocities. For the stretching deformation, the result is totally negative below 88 km and shows the most negative value of  $-0.08$  m/s/km at 80 km in January. In the upper altitude, the results are nearly negative in April to August and nearly positive in September to February, reaching  $0.05$  m/s/km at 96 km in February, which also corresponds to the maxima of the horizontal winds.

The relative vorticity in Figure 13e shows a clear stratification with height in summer and autumn, which is similar to the polar results reported by Chau et al. (2017). The value is negative between 84 and 92 km, with a maximum of  $-0.08$  m/s/km in August at 88 km, and is positive below or above this height range. The maximum positive value is  $0.18$  m/s/km in January at 96 km. Finally, the wind shearing deformation, as shown in Figure 13e, is close to 0 and even negative near the spring and autumn equinox, which corresponds exactly to the annual variation structure of the background mean winds. The minimum and maximum values are both at 88 km,  $-0.04$  m/s/km and  $0.09$  m/s/km, respectively, in March and December.

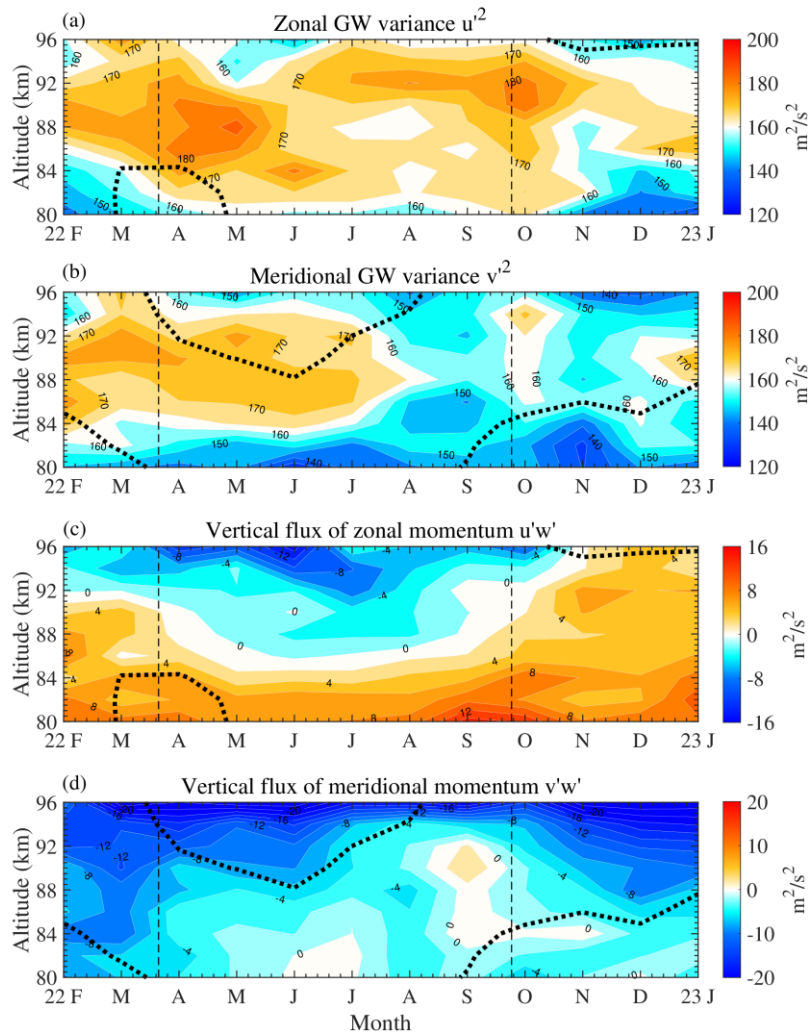


**Figure 14.** Height-time cross-sections of the zonal (a) and meridional (b) wind variance and the vertical flux of zonal (c) and meridional (d) momentum. Running averages over 30 days shifted by 7 days from February 2022 to February 2023. The black dashed lines indicate the zero mean zonal wind in (a) and (c) and zero mean meridional wind in (b) and (d).

Compared to monostatic meteor radar, more meteor detections and different viewing angles of the radial velocity observed by the bistatic meteor radar system can appreciably improve the precision of the GW covariance estimation (Spargo et al., 2019). In addition, we also try to use the bistatic meteor radar system to estimate the GW momentum fluxes, basically following the method introduced by Hocking (2005), Jia et al. (2018), Spargo et al. (2019) and the references therein. Figure 14 presents the seasonal variations in GW momentum flux terms.

As shown in Figures 14a and 14b, the zonal ( $u'^2$ ) and meridional ( $v'^2$ ) GW variance

terms generally increase with height below ~90 km and then decrease with height above 90 km, reflecting the characteristics of the GW amplitude variation. The zonal GW variances indicate a semiannual variation, with two maxima around April and October and two minima in August and December.

The meridional ( $v'^2$ ) GW variance mainly shows annual variation, with a maximum amplitude in winter and spring and a minimum amplitude in summer and autumn. Below 90 km, most gravity waves are unsaturated, so the amplitude of the gravity wave increases exponentially due to the decreasing air density, thus causing the GW variance to increase with height. Up to approximately 90 km, when the gravity wave is saturated, according to linear theory, the gravity wave will become unstable and break, leading to a decrease in the GW variance (Fritts, 1984; Placke et al., 2011).

In Figures 14c and 14d, the vertical fluxes of zonal ( $v'w'$ ) and meridional ( $u'w'$ ) momentum basically show a U-shape and an inverted U-shape, respectively. Both  $u'w'$  and  $v'w'$  decrease with height throughout the year, except for  $v'w'$  in September, when both reach maxima in September and minima in June but at different corresponding altitudes. Moreover, the meridional component appears to be southward during almost the whole year. These results are generally comparable with those of a previous study observed by Wuhan (30.2°N, 114.2°E) and Beijing (40°N, 116.3°E) at middle latitudes (e.g., Jia et al., 2018). Placke et al. (2011) reported that the GW activity in the upper mesosphere over Collm, Germany (51.31°N, 13.01°E) at higher-middle latitudes has a semiannual oscillation with the main maximum in summer and a minor maximum in winter. Combined with the background wind structure, we can see the influence of gravity waves on the structure of the background mean winds. From May to August, it can be considered that only the westward gravity wave can propagate upward under the background of the prevailing eastward wind, and the meanwhile, the westward momentum flux will produce the northward drag force under the action of the Coriolis force and thus slow down the southward wind.

**Comment:** Some aspects of the paper make me concerned that the analysis as presented has merit or was correctly applied. It is assumed that the vertical velocity can be ignored

in equations (7) and (8) without adequate justification.

**Response:** We have added the vertical velocity, and here, we focus only on the horizontal results, so we set the vertical velocity  $w = w_0$ . Many previous studies have estimated that the magnitude of the vertical velocity is just 0.1 cm/s to several m/s, which is far below the magnitude of the horizontal wind velocities (e.g., Vincent et al., 2019; Stober et al., 2022, and references therein). However, there were also some attempts to fit vertical winds to the observations (e.g., Chau et al., 2017; Conte et al., 2021; Chau et al., 2021), and the results may be contaminated by horizontal terms. Thereafter, we should note that the resulting vertical velocity presents not the real vertical wind but the so-called apparent vertical wind ( $w^*$ ) (Chau et al., 2017). The vertical velocity results of a few days and a year are shown in Figure R1. The estimated  $w^*$  presents a diurnal variation in Figure R1 (a) and shows a similar annual variation to that of the horizontal winds.

After revising equations (7) and (8), we have changed the corresponding contents of Figure 7 – Figure 12 in the revised manuscript. Although the overall change is small, we still find that the divergence decreases, which may lead to the large vertical velocity shown in Figure R1 (Chau et al., 2017).

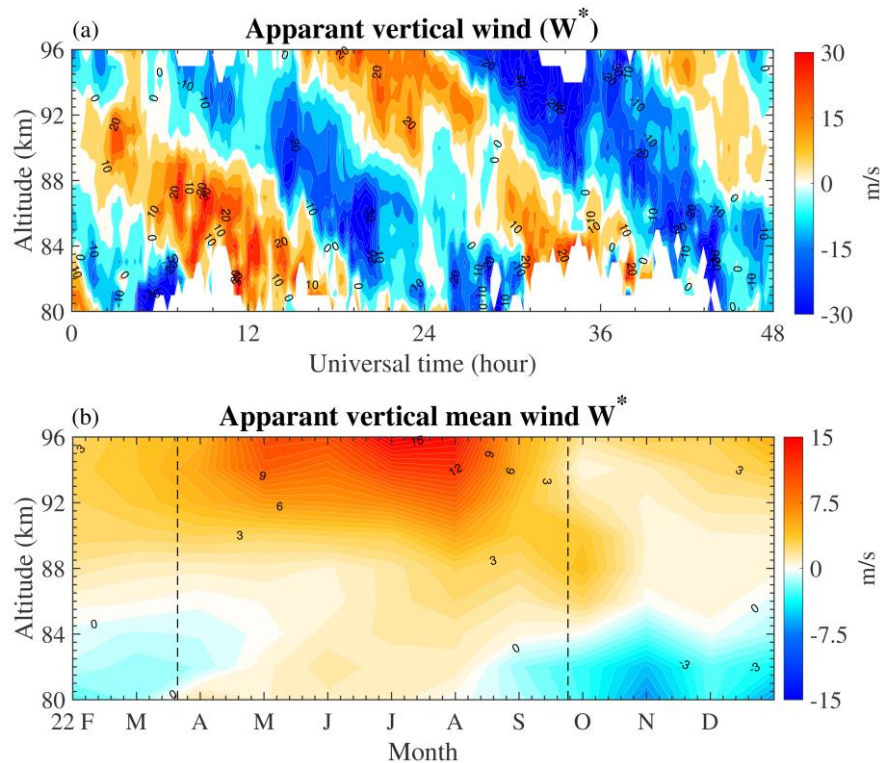


**Figure R1.** The vertical velocity of (a) October 16 and 17, 2021, and (b) February 1, 2022, to February 1, 2023. The thin black dashed lines in each panel present the equinoxes.

In the next stage, we will expand our multistatic meteor radar network in Central-Eastern China. The new multistatic meteor radar network will provide a better determination of vertical winds refer to the more recent results reported by Stober et al., (2021; 2022).

**Comment:** Differences in the winds portayed in Figure 6 approach 40 m/sec at heights where the meteor count rates should be large. Such large discrepancies between locations that are not far apart will need to be explained before readers can accept the more nuanced parameters describing velocity variations within the field.

The opportunities that will be afforded by the construction of a multi-radar array in central China are considerable but the above aspects of the analysis need to be resolved to ensure the results reflect true geophysical effects.

**Response:** The large discrepancies in Figure 6 may be generated for a few reasons. First, there are unevenly distributed meteors. Taking a look at Figure 5, we find that the distributions of the arrival angles of the two receiving sites are not totally the same. We select the angle data corresponding to the bins with sufficient meteors, compare these data of the two sites, and then find that most of the bins with large discrepancies in wind velocity have inconsistent angle distributions. Second, the distance between the two sites is 167.3 km, but the valid detection range of the Mengcheng site is just 150 km, so the observed fields are not the same. Once affected by strong atmospheric motions, it is possible to have large discrepancies. Third, most of the large discrepancies exist at 12 LT at lower/upper altitudes, and the meteors in this range are not sufficient to estimate accurate horizontal winds. Due to the combined influence of the above several factors, we believe our results are reasonable.

**References in this response:**

Chau, J. L., G. Stober, C. M. Hall, M. Tsutsumi, F. I. Laskar, and P. Hoffmann (2017), Polar mesospheric horizontal divergence and relative vorticity measurements using multiple specular meteor radars, *Radio Sci.*, 52, 811–828,



- doi:10.1002/2016RS006225. Stober, G., Chau, J. L., Vierinen, J., Jacobi, C., and Wilhelm, S.: Retrieving horizontally resolved wind fields using multi-static meteor radar observations, *Atmos. Meas. Tech.*, 11, 4891–4907, <https://doi.org/10.5194/amt-11-4891-2018>, 2018.
- Chau, J. L., Urco, J. M., Vierinen, J., Harding, B. J., Clahsen, M., Pfeffer, N., et al. (2021). Multistatic specular meteor radar network in Peru: System description and initial results. *Earth and Space Science*, 8, e2020EA001293. <https://doi.org/10.1029/2020EA001293>.
- Conte, J. F., Chau, J. L., Urco, J. M., Latteck, R., Vierinen, J., and Salvador, J. O.: First Studies of Mesosphere and Lower Thermosphere Dynamics Using a Multistatic Specular Meteor Radar Network Over Southern Patagonia, *Earth and Space Science*, 8, e2020EA001356, <https://doi.org/10.1029/2020EA001356>, 2021
- Poblet, F. L., Chau, J. L., Conte, J. F., Avsarkisov, V., Vierinen, J., & Charuvil Asokan, H. (2022). Horizontal wavenumber spectra of vertical vorticity and horizontal divergence of mesoscale dynamics in the mesosphere and lower thermosphere using multistatic specular meteor radar observations. *Earth and Space Science*, 9, e2021EA002201. <https://doi.org/10.1029/2021EA002201>.
- Spargo, A. J., Reid, I. M., and MacKinnon, A. D.: Multistatic meteor radar observations of gravity-wave–tidal interaction over southern Australia, *Atmos. Meas. Tech.*, 12, 4791–4812, <https://doi.org/10.5194/amt-12-4791-2019>, 2019.
- Stober, G., and J. L. Chau (2015), A multistatic and multifrequency novel approach for specular meteor radars to improve wind measurements in the MLT region, *Radio Sci.*, 50, 431–442, doi:10.1002/2014RS005591.
- Vierinen, J., Chau, J. L., Charuvil, H., Urco, J. M., Clahsen, M., Avsarkisov, V., et al. (2019). Observing mesospheric turbulence with specular meteor radars: A novel method for estimating second-order statistics of wind velocity. *Earth and Space Science*, 6. <https://doi.org/10.1029/2019EA000570>.
- Vincent, R. A., Kovalam, S., Murphy, D. J., Reid, I. M., and Younger, J. P.: Trends and Variability in Vertical Winds in the Southern Hemisphere Summer Polar Mesosphere and Lower Thermosphere, *J. Geophys. Res.-Atmos.*, 124, 11070–

## Tracked Changes

### Multistatic meteor radar observations of two-dimensional horizontal MLT wind

Wen Yi<sup>1,2</sup>, Jie Zeng<sup>1,2</sup>, Xianghui Xue<sup>1,2,3\*</sup>, Iain Reid<sup>4,5</sup>, Wei Zhong<sup>1,2</sup>, Jianfei Wu<sup>1,2</sup>, Tingdi Chen<sup>1,2</sup>, Xiankang Dou<sup>1,6</sup>

<sup>1</sup> Deep Space Exploration Laboratory / School of Earth and Space Sciences, University of Science and Technology of China, Hefei 230026, China

<sup>2</sup> CAS Key Laboratory of Geospace Environment/CAS Center for Excellence in Comparative Planetology, Anhui Mengcheng Geophysics National Observation and Research Station, University of Science and Technology of China, Hefei, China

<sup>3</sup> Collaborative Innovation Center of Astronautical Science and Technology, Harbin, China

<sup>4</sup> ATRAD Pty Ltd., Adelaide, SA 5000, Australia

<sup>5</sup> School of Physical Sciences, University of Adelaide, Adelaide, SA 5000, Australia

<sup>6</sup> Electronic Information School, Wuhan University, Wuhan, China

**Corresponding author:** Xianghui Xue ([xuexh@ustc.edu.cn](mailto:xuexh@ustc.edu.cn))

**Abstract:** All-sky meteor radars have become a reliable and widely used tool to observe horizontal winds in the mesosphere and lower thermosphere (MLT) region. The horizontal winds estimated by conventional single-station radars are obtained after averaging all meteor detections based on the assumption of the homogeneity of the horizontal wind in the meteor detection area (approximately 200-300 km radius). In this study, to improve the horizontal winds, we apply a multistatic meteor radar system consisting of a monostatic meteor radar in Mengcheng (33.36 °N, 116.49 °E) and a bistatic remote receiver in Changfeng (31.98 °N, 117.22 °E), separated by approximately 167 km to increase the number of meteors by at least 70% and provide

two different viewing angles of the meteor echoes. The accuracy of the horizontal wind measurement depends on the meteor number in time and altitude intervals. Compared to typical monostatic meteor radar, our approach shows the feasibility of estimating the two-dimensional horizontal wind field. The technique allows us to estimate the mean horizontal wind and the gradient terms of the horizontal wind, [moreover, as well as](#) the horizontal divergence, relative vorticity, stretching and shearing deformation of the wind field. [In addition, the seasonal variation in MLT dynamics parameters, including horizontal wind deformations and gravity wave \(GW\) momentum fluxes, in the MLT region at middle latitudes of the Northern Hemisphere are presented.](#) We are confident that the improved horizontal wind parameters will contribute to improving the understanding of the dynamics in the MLT region.

Keywords: Meteor radar, mesosphere and lower thermosphere region, horizontal wind

## **Introduction**

The mesosphere and lower thermosphere (MLT) are important connecting regions that couple the lower and upper atmosphere through a variety of atmospheric waves, such as gravity waves, tides and planetary waves (e.g., Salby, 1984, Fritts and Alexander, 2003; Forbes and Garrett, 1979). Observation of these atmospheric ~~dynamic~~[dynamical](#) processes is very important for understanding the coupling between atmospheric layers. In recent decades, significant development of ground-based techniques, such as radars and LIDARs, have permitted observations of MLT dynamics at different spatial and temporal scales, as well as their long-term climatology from the equator to the poles. In particular, meteor radar has become the most widely used instrument to routinely observe MLT winds among ground-based techniques because it has the advantages of being low cost and easy to install, and operate automatically and continuously under all weather conditions (e.g., Hocking et al., 2001; Holdsworth et al., 2004; Fritts et al., 2010; Yu et al., 2013; Jia et al., 2018; Spargo et al., 2019; Yi et al., 2016; 2019; 2021).

The radar technique for atmospheric wind measurement by detecting the radial drift velocity of the meteor ionized trail began in the 1950s, and within a few decades, pioneering studies of ~~the~~ mesospheric dynamics and their climatology were conducted (e.g., Robertson et al., 1953; Elford and Robertson, 1953; Elford, 1959; Roper and

Elford, 1963; Roper, 1966, 1975; ~~and~~ see Reid and Younger (2016) for a brief history of these early observations). From the late 1970s to the 1980s, the applications of meteor radar in mesosphere wind research diminished along with the retirement of some active researchers and important facilities; moreover, another radar technique using partial reflection operated in medium/high frequencies (M/HF) became more common (e.g., Reid, 2015). At the same time, a few interesting experiments using meteor trails to measure upper atmosphere winds were pioneered on the spaced antenna array of VHF (Very High Frequency) MST (Stratosphere, Troposphere, Mesosphere) and ST Doppler radars (e.g., Aso et al., 1979; Avery et al., 1983; Tsuda et al., 1987; Cervera and Reid, 1995; Hocking, 2011, and the references therein). However, all these early meteor radars suffer from low meteor detection rates. In the 1990s, the rebirth of meteor wind radar, also called all-sky meteor radar, was made possible by the development of inexpensive personal computers, solid-state radar transmitters and better data acquisition systems, as well as the interferometric technique of antenna configuration (e.g., Jones et al., 1998). In the 21<sup>st</sup> century, ~~the~~ meteor radar has become a standard tool for the routine measurement of the horizontal wind and dynamics in MLT and ~~has~~ largely displaced ~~the~~ previous instruments with similar functions, such as partial reflection radars (e.g., Vincent and Reid, 1983, Reid, 2015), ISR radar (e.g., Nicolls et al., 2010) and VHF Doppler radar (e.g., Reid et al., 1988).

A typical all-sky meteor radar consists of a pair of crossed dipoles (e.g., Hocking et al., 2001; Holdsworth et al., 2004) or a group of a few transmitting elements for transmission (e.g., Fritts et al., 2010; 2012) collocated with five pairs of crossed dipoles arranged in a cross as an interferometric receiving antenna array (e.g., Jones et al., 1998). This configuration is also called monostatic or single-station meteor radar and observes the backscatter meteor echo. The winds are estimated by monostatic meteor radar assuming that the horizontal wind is homogeneous inside the meteor detection volume (approximately 200–300 km radius). The wind measurements normally have spatial and temporal bins of 2-3 km and 0.5-2 hours in the approximate altitude range of 70–110 km, respectively. These measurements have made significant contributions to understanding the behaviour of large-scale atmospheric waves, such as planetary waves

(e.g., Vincent, 2015 and the references therein) and tides (e.g., Manson et al., 2002; Jacobi, 2012; Stober et al., 2021a)) in the MLT region. In addition, although there is some controversy concerning the accuracy and composite temporal window (e.g., Vincent et al., 2010; Fritts et al., 2012), monostatic meteor radars have been developed to estimate gravity wave momentum fluxes because of substantial continuous data all over the world (e.g., Hocking et al., 2005; Fritts et al., 2010., Andrioli et al., 2013; Jia et al., 2018, and references therein).

In addition to the now dominant all-sky monostatic (backscatter) meteor radar, early meteor radars were designed as ~~multi-station~~multistation systems using forward scattering meteor echoes. This was because these early radars operated as continuous wave radars, requiring separation between the transmitter and receivers. For example, a famous meteor radar was built to measure the upper atmosphere wind in 1958 at the St Kilda site, near Adelaide. This radar system consisted of a transmitting station and a remote receiving system approximately 23 km from the transmitter, and the receiving system had a main site and two supplementary receiving sites approximately 5 km north and east (Roper and Elford, 1963; Roper, 1966). A similar meteor radar system with a 27 km distance between the transmitting station and receiving station was installed in Atlanta, GA, USA (e.g., Roper, 1975). Since then, however, this type of radar has gradually been replaced by monostatic narrow beam (e.g., Cervera and Reid, 1995) and then all-sky (e.g., Hocking et al., 2001; Holdsworth et al., 2004) radars for measuring MLT region dynamics. Recently, some innovative multistatic meteor radar systems, such as the MMARIA (multistatic and multifrequency agile radar for investigations of the atmosphere) (Stober and Chau, 2015; Stober et al., 2018), SIMO (single-input multiple-output) (Spargo et al., 2019), and SIMONe (Spread Spectrum Interferometric Multistatic meteor radar Observing Network) (Conte et al., 2021; Chau et al., 2021), have been designed and proven to increase the number of meteor detections and the diversity of viewing velocity angles. Thus, multistatic meteor radar systems have several advantages over classic monostatic meteor radars, such as obtaining higher-order wind field information (e.g., Stober et al., 2015; 2018, Chau et al., 2017), vertical velocity (e.g., Chau et al., 2021; Stober et a., 2022) and mesoscale dynamics (e.g.,

Spargo et al., 2019; Conte et al., 2021; Volz et al., 2021; Stober et al., 2021b).

This study describes a multistatic meteor radar system consisting of a monostatic meteor radar and a bistatic remote receiver separated by 167 km and presents preliminary results of the derived two-dimensional wind fields in the MLT region over Central-Eastern China. Our paper is organized as follows. In section 2, we present the experimental instruments and their arrangement. Then, in section 3, we introduce the measurements obtained by the radar system. The preliminary results of improved wind estimations are presented in section 4. Finally, we summarize our results and discuss multistatic meteor radar system expansion in the future.

## 2 Instrumentation and Data

The multistatic meteor radar considered in this study consists of a meteor radar located at Mengcheng (33.4 N, 116.3° E) and a remote receiving system located at Changfeng (31.98° N, 117.22° E) in Hefei city, Anhui Province. Figure 1 shows the schematic diagram of the backward and forward scatter geometry for the Mengcheng meteor radar and the Changfeng remote receiver, hereafter MCR and CFR. The Changfeng remote receiver is located southeast of Mengcheng, and the distance between the two sites is approximately 167.6 km.

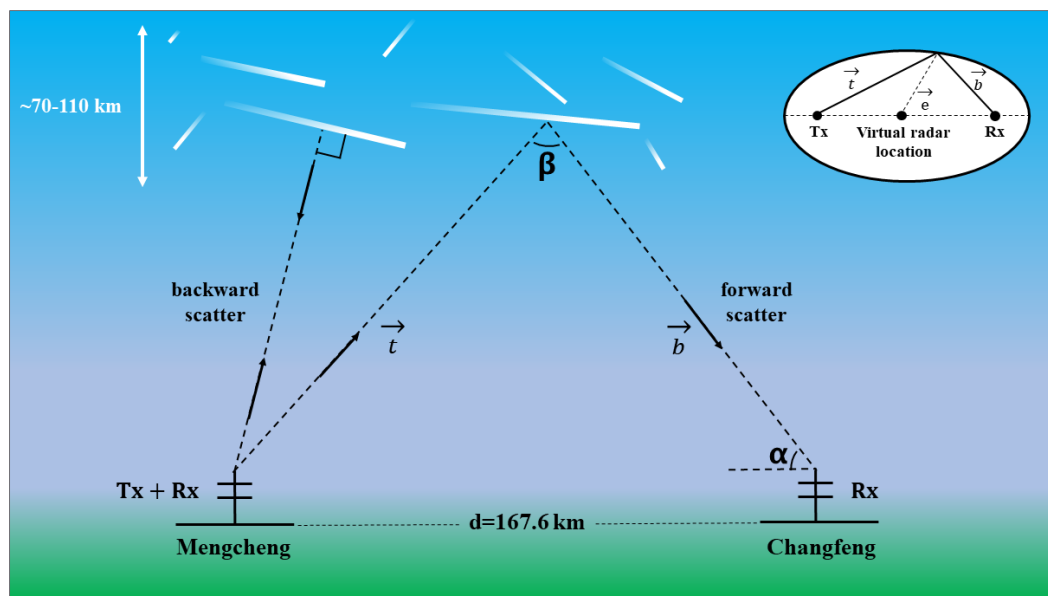


**Figure 1.** Schematic diagram of a backward scatter and forward scatter geometry for the Mengcheng meteor radar and Changfeng remote receiver.

**Table 1.** Main operation parameters of the Mengcheng meteor radar

Frequency	38.9 MHz
Peak power	20 kW
Pulse repetition frequency (PRF)	430 Hz
Coherent integrations	4
Range resolution	1.8 km
Pulse type	Gaussian
Pulse code	4 bit complementary
Pulse width	24 $\mu$ s
Duty cycle	15%
Detection range	70-110 km

The Mengcheng all-sky meteor radar (MCR) has been operating since April 2014, at a frequency of 38.9 MHz, and a peak power of 20 kW. The Mengcheng meteor radar belongs to the meteor detection radar (MDR) series manufactured by ATRAD and is similar to the Buckland Park meteor radar system described by Holdsworth et al. (2004). A single crossed and folded dipole is used for transmission. Five two-element Yagi antennas using a cross ‘+’ shape arrangement (Jones et al., 1998) are used for reception. Table 1 shows the experimental parameters used for the Mengcheng meteor radar transmitter.

The Changfeng remote receiver system consists of five receiver antennas using a ‘T’ shaped arrangement (Jones et al., 1998), a digital transceiver identical to the Mengcheng meteor radar. To permit accurate range and Doppler estimates at the remote site, the system timing, frequency, and clocks at both sites are synchronized with GPS-disciplined oscillators (GPSDOs). The techniques used to estimate various data products from the received meteor echoes, including radial velocity, meteor position, and decay time, follow those outlined in Holdsworth et al. (2004a). Both radars belong to and are operated by the University and Science and Technology of China (USTC). [The dataset considered spans 6 days from 15 October to 20 October 2021. The Mengcheng and Changfeng bistatic meteor radar system was completed in October 2021, but it was not regularly observed until February 2022 due to site maintenance. The dataset in this study considered spans October 2021 to February 2023, with a major discontinuity from November 2021 to January 2022.](#)

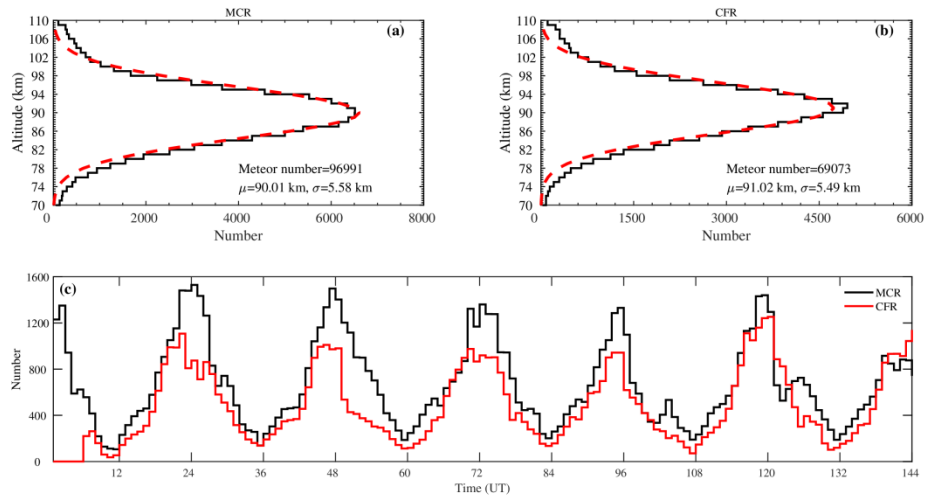
带格式的: 字  
带格式的: 字  
色: 黑色

### 3 Observations

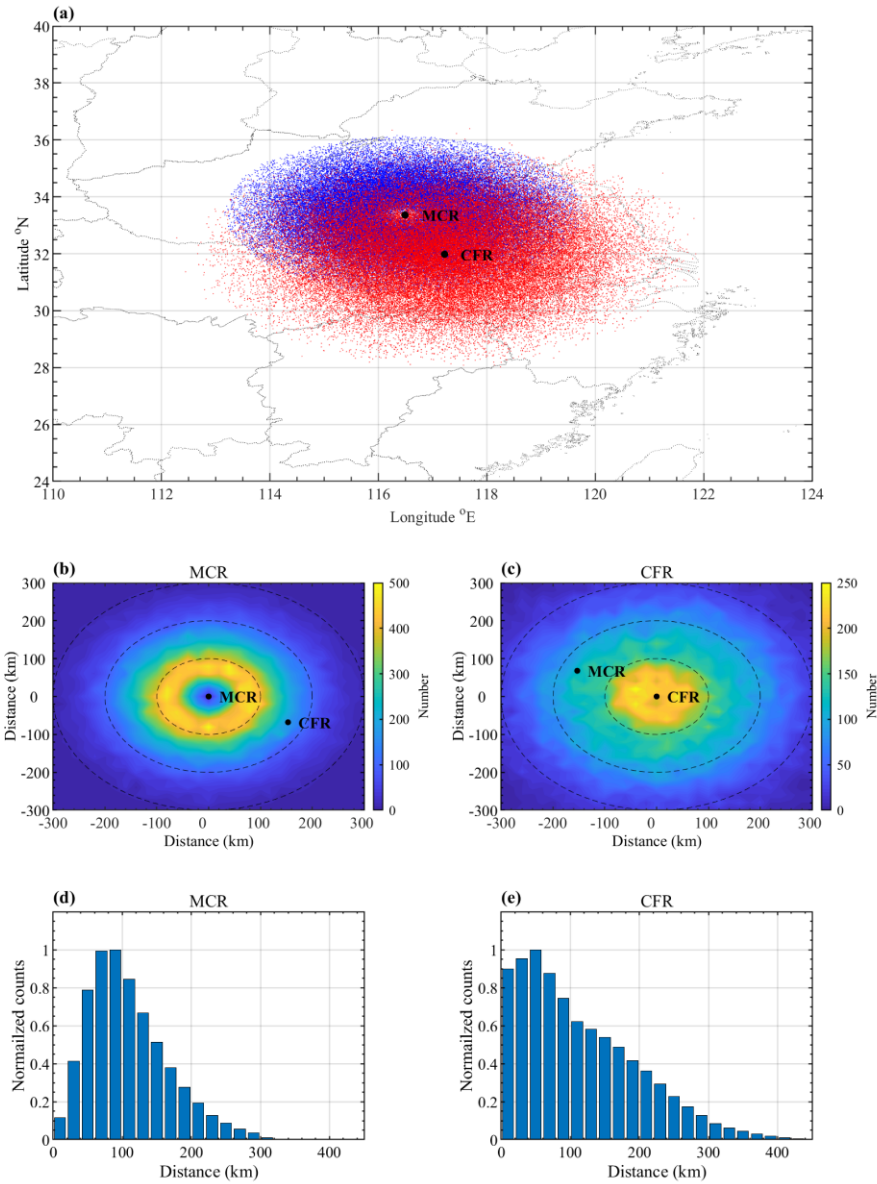
Figures 2a and 2b show the histograms of [the](#) meteor height distribution observed by the MCR and CFR, which are well approximated by a fitted Gaussian curve (as shown by red dashed curves). The peak heights of the meteor height distribution observed by MCR and CFR are approximately 90 and 91 km, respectively. The peak height of the CFR appears to be 1 km higher than that of the MCR because the equivalent frequency or effective Bragg wavelengths for the forward scatter of the CFR would be lower than those for the backscatter detected by the MCR. The results of the equivalent frequency will be presented later. Figure 2c shows that the hourly meteor number observed by the MCR is larger than that of the CFR. The meteor number of the forward scatter observed by the CFR is approximately 71% of the detections using backscatter by the MCR monostatic system. These results are similar to the results from two bistatic meteor radar systems reported by Stober et al. (2015) and Spargo et al. (2019). In addition, the meteor count rates observed by the MCR and CFR both show a clear diurnal variation, with a high count rate in the local morning (i.e., 2000-0004 UT) and a low count rate during local night (i.e., 8000-1600 UT).

Figure 3 shows the projection of meteor detections observed by the MCR and CFR on a plan view map. Figure 3a shows a reasonable overlap of meteor detections over the two receiving sites. In Figures 3b and 3d, the backscattered echoes are observed in a roughly circular region with an approximately 300 km radius and are mainly distributed 50-120 km from the MCR receiver. In Figures 3c and 3e, the forward scatter meteor echoes observed by the CFR are more widely and evenly distributed than those observed by single-station radar, and the meteors are mainly distributed within a circular region of radius of [about](#)[approximately](#) 100 km to the CFR.





**Figure 2.** The height distribution of meteor detections in 1 km bins during October 15-20, 2021, [observed](#) by (a) Mengcheng and (b) Changfeng receivers. The fitted Gaussian curves used for the estimation of peak height ( $\mu$ ) and standard deviation ( $\sigma$ ) of [the](#) meteor height distribution. (c) Hourly meteor numbers observed by the Mengcheng (black line) and Changfeng (red line) radars.



**Figure 3.** (a) Two-dimensional projection of meteor detections observed by [the](#) Mengcheng (blue dots) and Changfeng (red dots) receivers. Horizontal distribution of meteors for the (b) Mengcheng and (c) Changfeng receivers. Histograms of [the](#) meteor number ratio versus distance observed by the (d) Mengcheng and (e) Changfeng receivers. The distance represents the horizontal distance from the projection of meteor echoes to receivers.

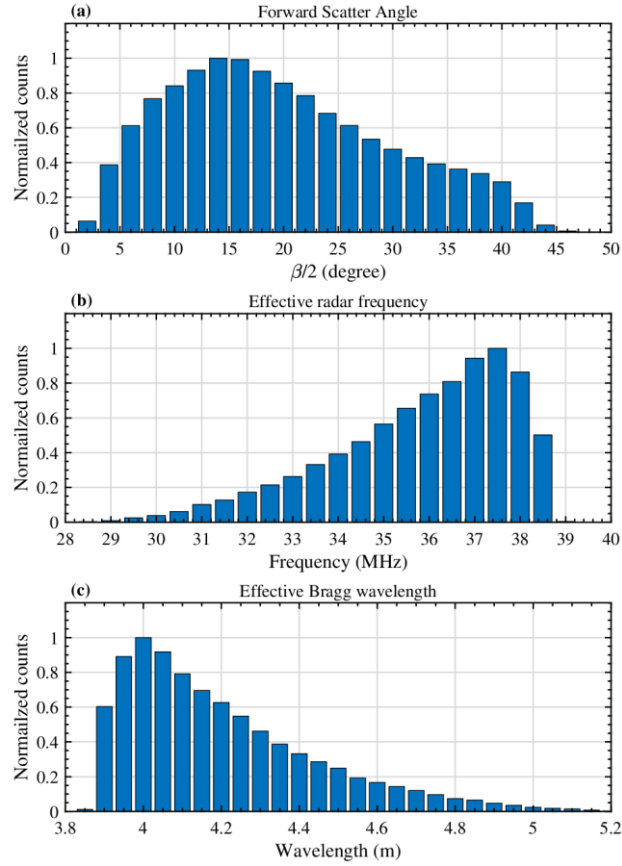


**Figure 4.** Histograms of detections as a function of (a) forward scatter angle, (b) equivalent frequencies and (c) effective Bragg wavelength for the Changfeng remote receiver.

Returning now to the geometrical relationship shown in Figure 1,  $\vec{t}$  and  $\vec{b}$  represent the vectors from the MCR transmitter to meteor and the meteor to the CFR receiver, respectively.  $\vec{d}$  represents the straight line from the MCR transmitter to the CFR receiver. The angle of arrival (AOA, i.e., zenith and azimuth) for the CFR remote receiver can be calculated by using the phase differences between the interferometric antennas. However, the angle ( $\alpha$ ) between the scatter wave ( $\vec{t}$ ) and  $\vec{d}$  (the straight line from the MCR to CFR) has a small difference from the elevation angle of the scatter wave because of the Earth's curvature. This small difference can be calculated using the geometry of Earth's curvature and radius and the location of the transmitter and receiver. Then, the path length of incident and scattered waves can be calculated using

Equation (1) (Doviak and Zrnic, 2006).

$$|\vec{t}| = \frac{R_i^2 - |\vec{d}|^2}{2 \cdot (R_i - |\vec{d}| \cos(\alpha))}, \quad (1)$$

where  $R_i$  is the range of total wave path  $R_i = |\vec{t}| + |\vec{b}|$  from the MCR transmitter to the meteor trail and to the CFR receiver.  $R_i$  is given by  $R_i = R + iR_{amb}$ ,  $R_{amb} = c/(2 \cdot PRF)$  is the maximum unambiguous range,  $c$  is the speed of light, PRF for the Mengcheng meteor radar is 430 Hz, and the typically unambiguous number  $i=0, 1, 2, \dots$ . Therefore, for the Mengcheng meteor radar, the maximum echo range is  $R_{amb} = 349$  km, and the unambiguous number is estimated using  $i=0$  or 1 (e.g., Holdsworth et al., 2004).

$$\beta = \cos^{-1} \left( \frac{\vec{t} \cdot \vec{b}}{|\vec{t}| |\vec{b}|} \right), \quad (2)$$

The forward scatter angle can be estimated by using equation (1) (e.g., Stober et al., 2018, Spargo et al., 2019). As shown in Figure 4a, the forward scatter angle ( $\beta/2$ ) values vary between  $0^\circ$  and  $50^\circ$ . The lower value of the forward scatter angle is close to  $0^\circ$ ; in this case, the scattering geometry is similar to that of the backscatter model. The larger value of  $50^\circ$  corresponding to the meteor trail is between the MCR transmitter and CFR receiver at 70 km altitude. The meteor trails are concentrated at approximately  $15^\circ$ , which means that the meteor trails are mainly distributed over the CFR receiver.

Figure 4b shows the distribution of equivalent frequencies corresponding to the meteor trail observed by the Changfeng receiver. The equivalent frequencies show a peak at approximately 37.5 MHz, which is 1.4 MHz lower than the Mengcheng transmitted frequency (38.9 MHz). The lowest equivalent frequencies are approximately 28.5 MHz, so the frequency bandwidth is approximately 10.4 MHz. This result explains why the peak of the meteor height distribution observed by the CFR receiver is approximately 1 km higher than that of the backscatter meteor trails observed by the MCR receiver (Ceplecha et al., 1998; Yi et al., 2018). Stober and Chau (2015) transmitted two frequencies at 32.55 MHz and 53.5 MHz and observed by a 118 km remote receiver with two peak (bandwidth) frequencies at approximately 31 (5.5) MHz and 49 (10.5) MHz, respectively. This finding is consistent with the suggestion that a higher

transmitter frequency gives a wider equivalent frequency bandwidth (e.g., Stober et al., 2015).

The projected velocity of the meteor trail observed by the remote station is considered along the Bragg wave vector (*de Elia and Zawadzki, 2001*). Therefore, for the forward scatter geometry, the direction of the radial drift velocity of the meteor trail represents the Bragg wave vector, i.e.,  $\vec{e}_B$  shown in Figure 1 (e.g., Stober et al., 2015; Spargo et al, 2019). The Bragg wave vector  $\vec{e}$  can be obtained as  $\vec{e} = \frac{\vec{t} - \vec{b}}{|\vec{t} - \vec{b}|}$ . In the case of the backward scatter geometry based on the monostatic meteor radar, the direction of the radial drift velocity is perpendicular to the meteor trail. The Bragg wavelengths of backscatter are  $\frac{\lambda}{2} = 3.86$  m. For the forward scatter geometry, the Bragg wavelengths are given by

$$\lambda_B = \frac{\lambda}{2\cos(\beta/2)}, \quad (3)$$

In Figure 4c, the Bragg wavelength distribution shows a peak at approximately 4 km with a bandwidth of approximately 1.4 m. The radial drift velocity projected along the Bragg wavelengths measured by the remoter receiver can be expressed as

$$v_B = f_d \lambda_B, \quad (4)$$

where  $f_d$  is the Doppler frequency shift. In the case of backward scatter geometry, the radial velocity is perpendicular to the meteor trail and is  $v_B = f_d \lambda / 2$ .

Figure 5 shows the angle of arrival (zenith and azimuth) of meteor echoes and the Bragg vector observed by the Mengcheng and Changfeng receivers, respectively. The angles of arrivals observed by the MCR and CFR receivers are basically a similar distribution, the zenith angles are mainly distributed from 45°-70°, and the azimuth angles are relatively evenly distributed, with a slightly greater number in the area north (i.e., 350°-20°) of the receivers. The bistatic meteor radar distribution provides a large increase in scattering detections per unit time along with observations of the same volume from different viewing angles.

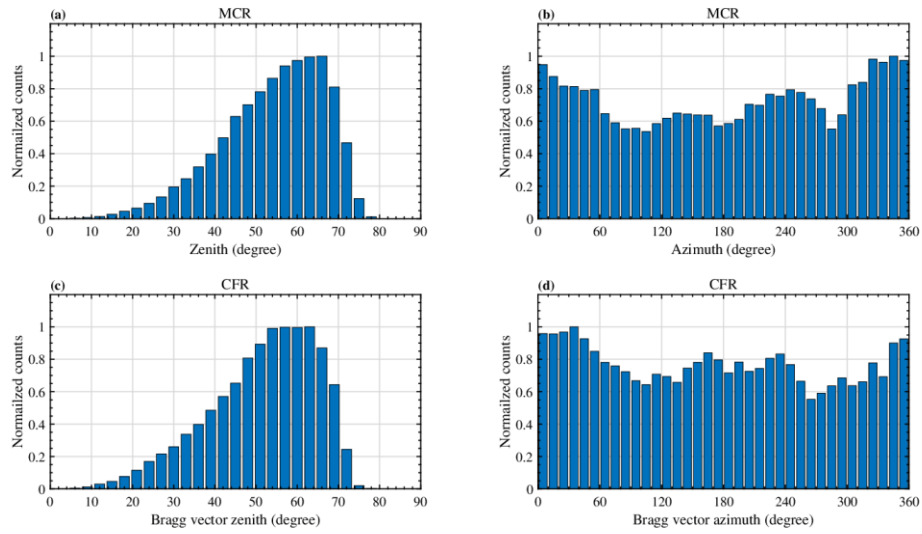


**Figure 5.** Histograms of (a) zenith and (b) azimuth of meteor echoes observed by the Mengcheng (upper) and the (c) zenith and (d) azimuth of the Bragg vector observed by the Changfeng (lower) receivers.

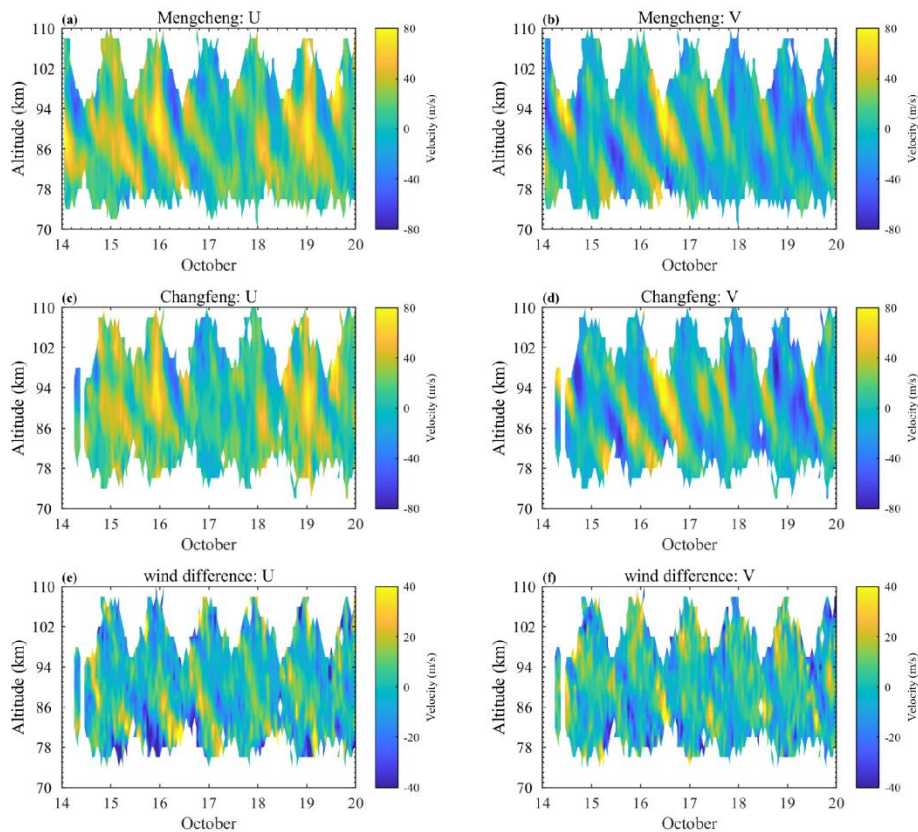


**Figure 6.** Contour plots of (right) zonal and (left) meridional hourly mean winds observed by the (upper) Mengcheng and (middle) Changfeng receivers and (lower) the

wind differences between the Mengcheng and Changfeng measurements.

Given the angle of arrival and radial velocity, the averaged horizontal wind can be estimated by both monostatic and remote receivers. Figure 6 shows the comparison of the hourly averaged horizontal (zonal and meridional) winds observed by the MCR and CFR. The zonal and meridional mean winds all show dominant diurnal (24 h) variations with a clear upward propagating phase. In Figures 6e and 6f, the wind differences between the two measurements still show a weak tidal structure, which may be because the tidal waves over the two receiver sites are different and the two receivers measuring different viewing areas of the atmosphere make slightly different geophysical waves, especially tidal waves. A comparison study to discuss tidal differences observed by the bistatic meteor radar described in this study and the Kunming two collocated meteor radar at Kunming meteor radar (Zeng et al., 2022) is [working on-being performed](#). This provides an exploration of the viewing geometry and geophysical volume, and the diurnal variation [of in](#) the meteor count [effecting on-affecting](#) tide estimation. However, [a](#) discussion of these [differeneedifferences](#) is beyond the scope of the present study and will be discussed in future papers.

#### **4. Two-dimensional horizontal wind observed by the bistatic meteor radar**

The averaged wind components are generally calculated by applying a so-called all-sky method under the assumption of a homogeneous wind field (e.g., Hocking et al., 2001, Holdsworth et al., 2004). The multistatic geometry allows the investigation of nearly the same phenomenon from different angles and volumes and thus makes it possible to reveal the inhomogeneities of the wind fields. Browning and Wexler (1968) introduced the velocity azimuth display (VAD) method for situations in which the wind field is not horizontally uniform, applying a linearity hypothesis to acquire the horizontal winds with their derivatives. Waldteufel and Corbin (1979) proposed the volume velocity processing (VVP) method, making full use of the meteor echoes within the observation volume to obtain the linear wind field. The difference between these two approaches mainly lies in the idea of solving equations. Stober et al. (2013) compared both methods in terms of gravity wave detection and found no distinct difference between them. In this study, we apply the VVP method to retrieve the horizontal winds.

According to the VVP method, the wind components of the scatter motion  $V = (u, v, w)$  can be described linearly by

$$\begin{aligned} u(x, y, z) &= u_0 + \frac{\partial u}{\partial x}(x - x_0) + \frac{\partial u}{\partial y}(y - y_0) + \frac{\partial u}{\partial z}(z - z_0), \\ v(x, y, z) &= v_0 + \frac{\partial v}{\partial x}(x - x_0) + \frac{\partial v}{\partial y}(y - y_0) + \frac{\partial v}{\partial z}(z - z_0), \\ w(x, y, z) &= w_0 + \frac{\partial w}{\partial x}(x - x_0) + \frac{\partial w}{\partial y}(y - y_0) + \frac{\partial w}{\partial z}(z - z_0), \end{aligned} \quad (6)$$

where  $(x, y, z)$  are the coordinates in the Cartesian reference frame and  $(u_0, v_0, w_0)$  is the mean wind at a fixed point  $(x_0, y_0, z_0)$ . In stratiform situations, it is appropriate to ignore  $\frac{\partial w}{\partial x}$  and  $\frac{\partial w}{\partial y}$  with respect to  $\frac{\partial u}{\partial z}$  and  $\frac{\partial v}{\partial z}$  (Waldteufel and Corbin, 1979). Here, we only focus on the horizontal components; thus, we assume  $\frac{\partial w}{\partial z} = 0$  for the simplicity of the equations and obtain

$$\begin{aligned} u(x, y, z) &= u_0 + \frac{\partial u}{\partial x}(x - x_0) + \frac{\partial u}{\partial y}(y - y_0) + \frac{\partial u}{\partial z}(z - z_0), \\ v(x, y, z) &= v_0 + \frac{\partial v}{\partial x}(x - x_0) + \frac{\partial v}{\partial y}(y - y_0) + \frac{\partial v}{\partial z}(z - z_0), \\ w(x, y, z) &= w_0. \end{aligned} \quad (7)$$

The radial velocity can be expressed as

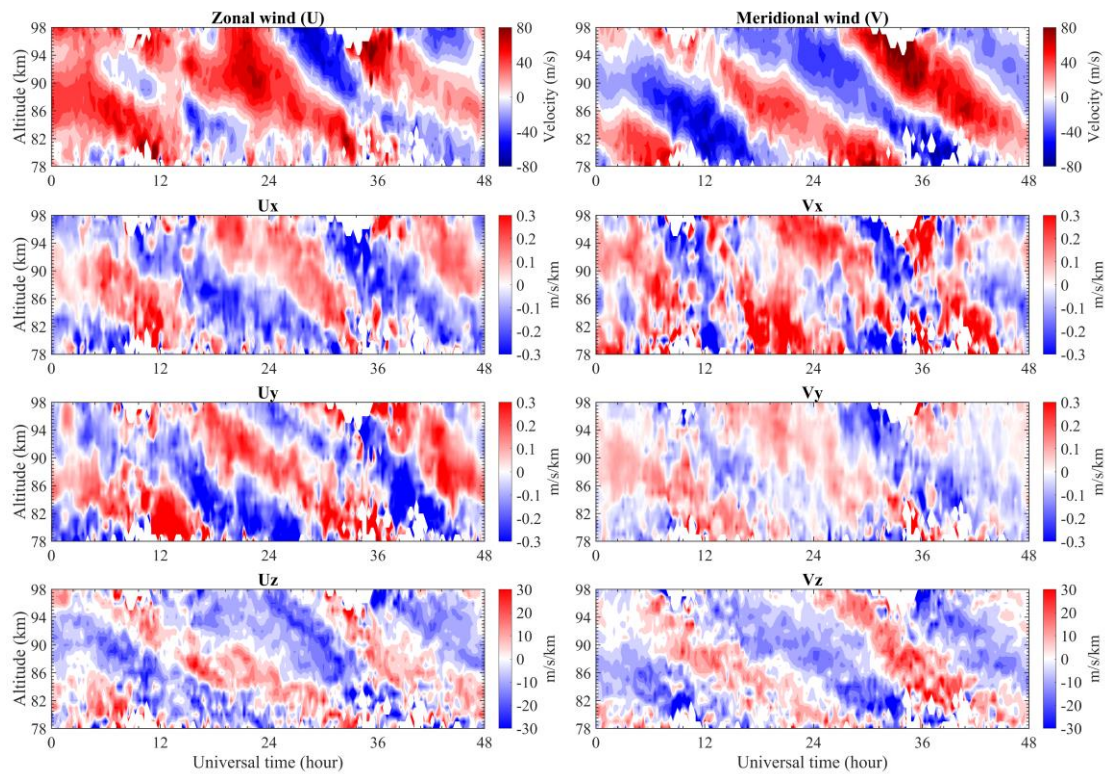
$$V_r = u \sin \phi \sin \theta + v \cos \phi \sin \theta + w \cos \theta, \quad (8)$$

where  $\theta$  and  $\phi$  are the zenith and azimuth angles, respectively. Using the least square method, the mean winds and the inhomogeneities of the winds (such as the horizontal divergence  $(\frac{\partial u}{\partial x} + \frac{\partial v}{\partial y})$ , relative horizontal vorticity  $(\frac{\partial v}{\partial x} - \frac{\partial u}{\partial y})$ , stretching  $(\frac{\partial u}{\partial x} - \frac{\partial v}{\partial y})$  and shearing  $(\frac{\partial u}{\partial y} - \frac{\partial v}{\partial x})$  [deformations](#) can be easily achieved due to the large number of meteor echoes detected in the selected volume.

We set the MCR and CFR as the origins of the two local ENU coordinates, and for the convenience of the calculation, we assume the midpoint of the two stations as the fixed point, that is,  $(x_0, y_0) = (x_{mid}, y_{mid})$ , and  $z_0$  is the reference altitude, normally ranging from 70 km to 110 km. The meteor locations  $(x_m, y_m, z_m)$  in both ~~two~~-local ENU ~~coordinate~~[coordinates](#) are calculated using the detected range and arrival angle, and then considering the curvature of the Earth, we conduct transformations as described by Stober et al. (2018). First, we transform the meteor location  $(x_m, y_m, z_m)$



into the ECEF coordinates  $(X_M, Y_M, Z_M)$ . Then, convert the ECEF coordinates  $(X_M, Y_M, Z_M)$  into geodetic coordinates  $(\phi_m, \lambda_m, h_m)$ . Finally, the local ENU coordinates of meteor echoes to the midpoint can be calculated as  $(x'_m, y'_m, z'_m)$ . We conduct 2-D wind fitting by shifting a [3 km, 1 h] window by a [1 km, 0.25 h] step. The windows are centered at the interested height and time of interest, containing no less than 10 meteors for the accuracy of the retrieval. Then, using the meteor information relative to the two stations and applying the least squares method, the 8 unknowns in Equation (7) can be retrieved, and we can select the area of interest to estimate the local wind fields. Note that the 8 unknowns are corresponding to the whole area, and the local winds are calculated using Equation (6) for a given point  $(x, y, z)$ .



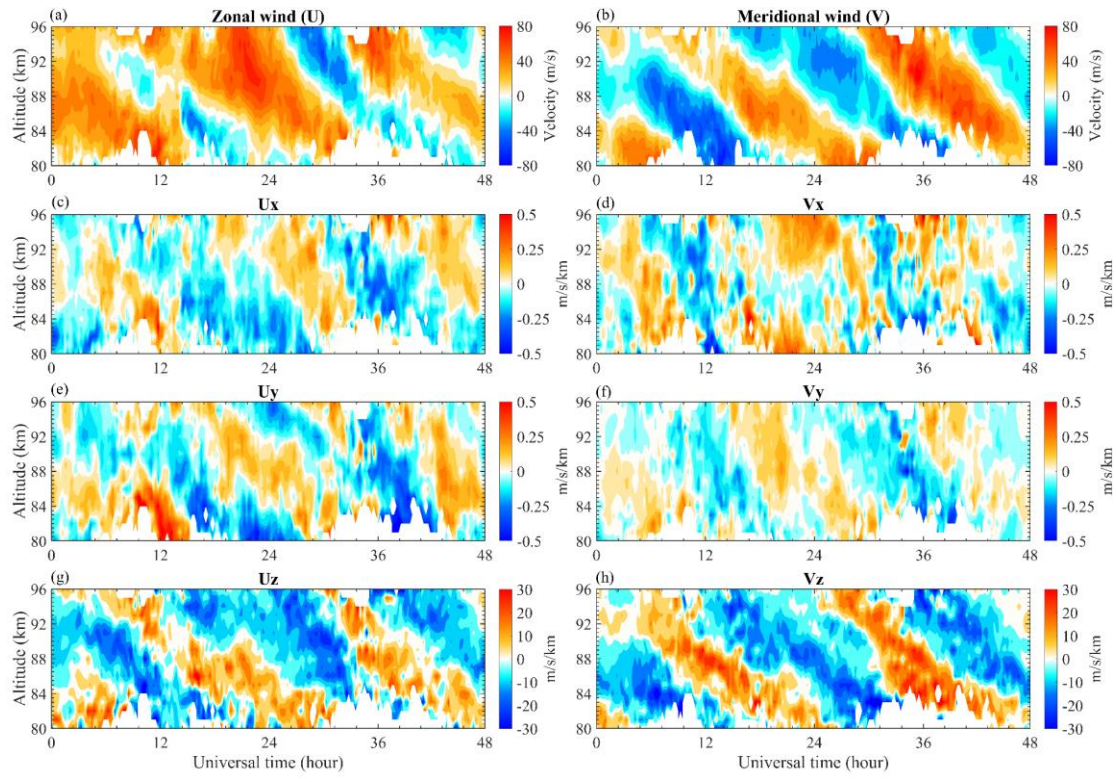
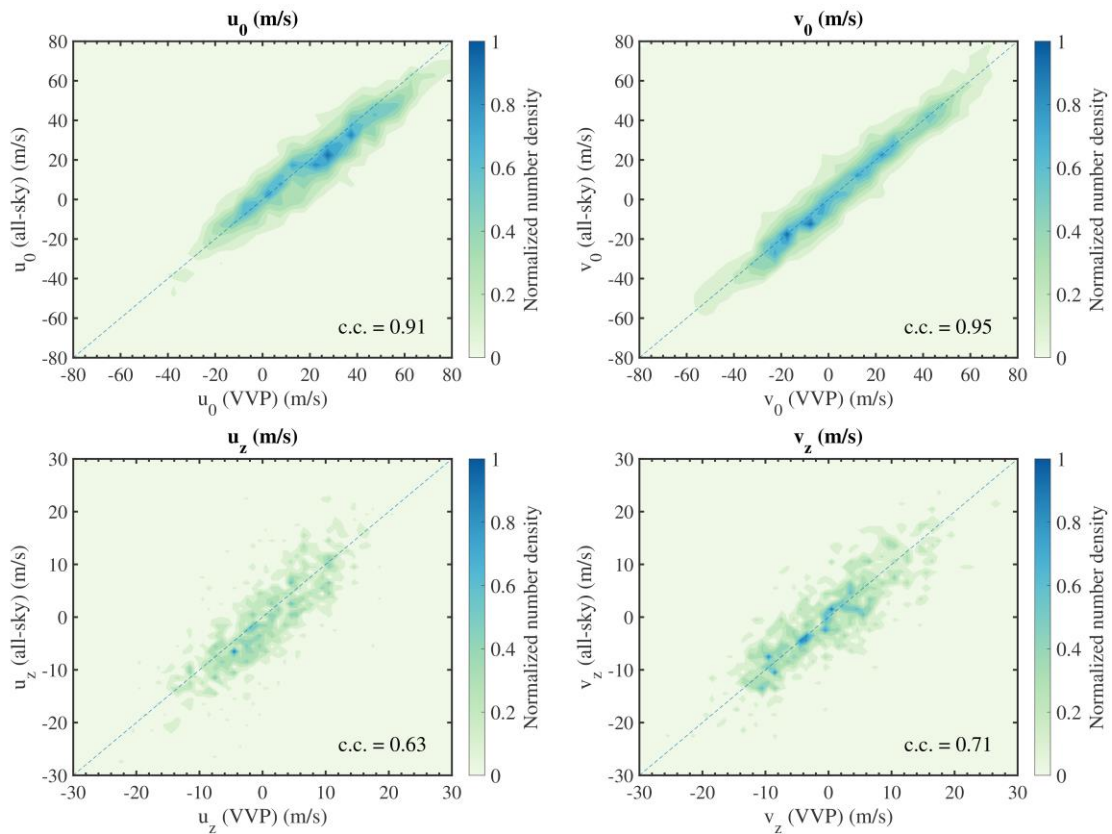


**Figure 7.** Mean horizontal winds and the gradient terms of the MLT wind fields on October 16 and 17, 2021. The left side represents the zonal component, and the right side represents the meridional component.—

Figure 7 shows the mean winds ( $u_0$ ,  $v_0$ ) and the gradient terms ( $u_x$ ,  $u_y$ ,  $u_z$ ,  $v_x$ ,  $v_y$ ,  $v_z$ ) of the horizontal wind fields on October 16 and 17, 2021, retrieved using the MCR-CFR composite [data sets](#). These 8 parameters are fitted using Equations (7) and (8) with the meteor information, which is the location of the meteors relative to the MCR and the corresponding radial velocity vector of the CFR output. The mean winds present diurnal tidal [structures](#), and their horizontal and vertical gradient terms also show distinct diurnal signatures, [though](#)  $v_x$  seems to show diurnal/semidiurnal features below/above 84 km. The magnitude of the gradient terms is nearly the same, and the values of  $v_y$  are [relatively](#) smaller. Chau et al. (2017) calculated the wind parameters in [the](#) polar region and exhibited similar [semi-diurnal](#) results.

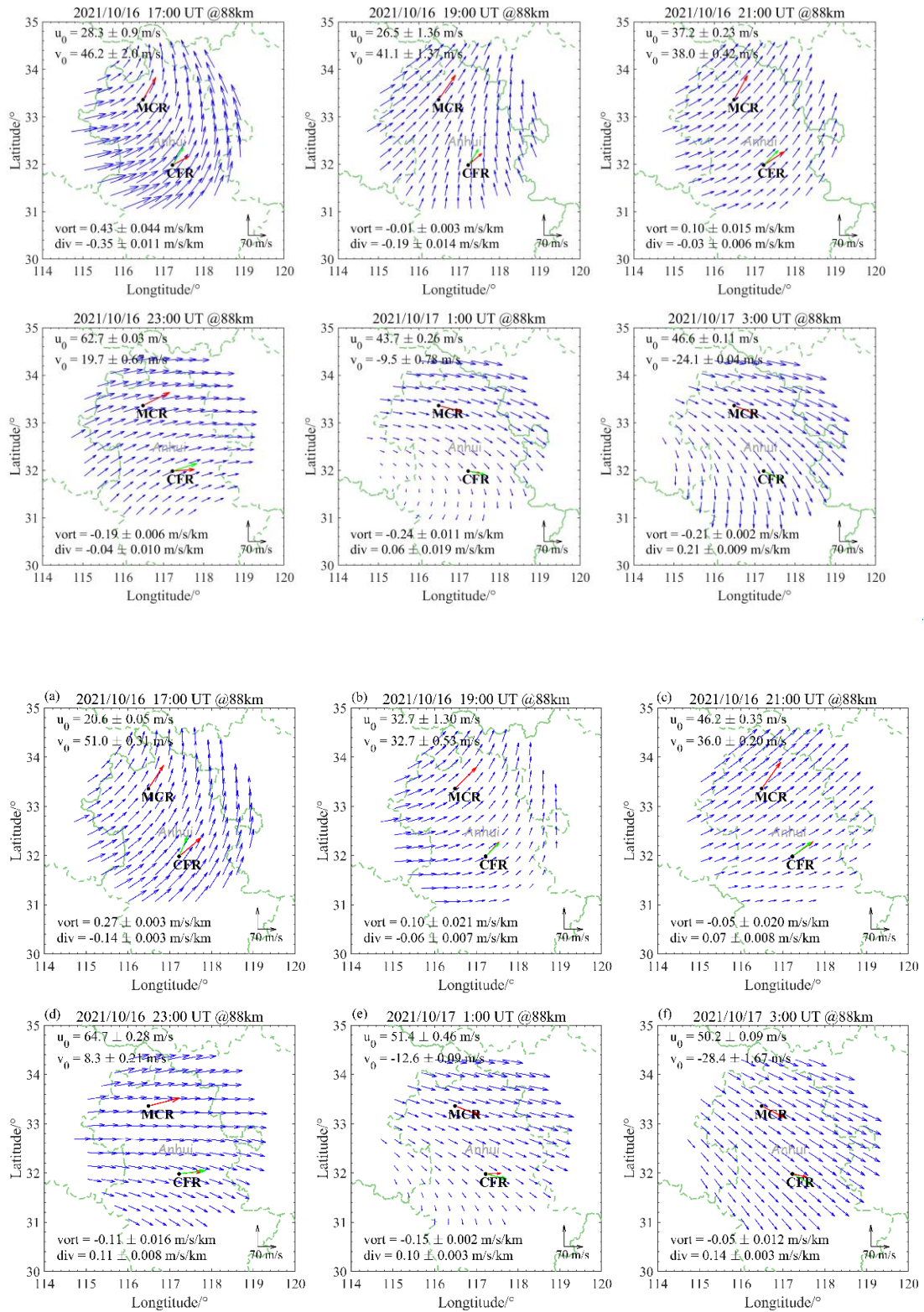
[In order to](#) verify the reliability of our results, we compared the traditional all-sky results and the VVP results by calculating the correlation coefficients and the regional

winds. The correlation coefficients are shown in Figure 8. The upper row shows the VVP mean winds versus the all-sky mean winds, and the bottom row shows the VVP vertical gradients versus the calculated all-sky vertical gradients using the mean winds from the adjacent time-height bins. The correlation between the mean winds retrieved by these two methods is higher than 0.9, illustrating high consistencies, and the correlations between the computed  $u_z$ ,  $v_z$  and the calculated derivative of horizontal winds in [the](#) vertical direction are also appreciable, both verifying the reliability of the gradient results using [the](#) VVP method. [Besides](#)[In addition](#), by careful observation of the normalized density distribution, we find [that](#) the meridional terms ( $u_z$ ,  $v_z$ ) are more symmetrically distributed.



**Figure 8.** The correlation coefficients between the VVP method (x-axis) and the all-sky method (y-axis). The upper row shows the mean zonal wind and mean meridional wind correlations, and the bottom row shows the correlation of vertical gradients of zonal and meridional wind components. The dashed blue line represents  $x=y$ . The blue-green blocks are the normalized number density. The values of correlation coefficients

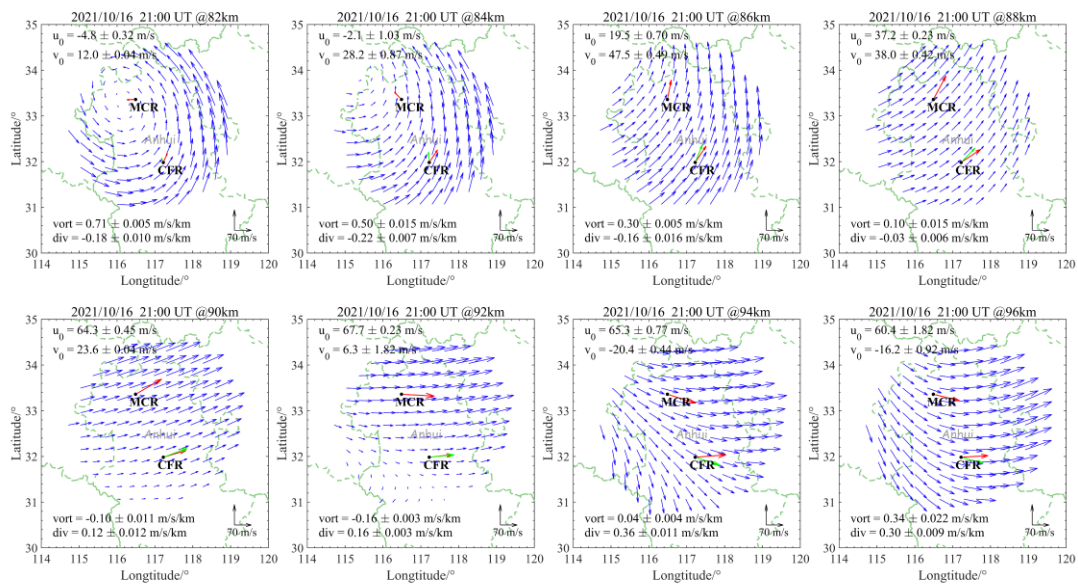
are labelled respectively.



**Figure 9.** Hourly wind fields at 88 km from 1700 UTC on 16 October 2021 to 0300 UTC on 17 October 2021. The green dashed line shows the provincial boundaries of

Anhui Province. The blue arrows represent the wind vectors. The red and green arrows represent the horizontal mean winds calculated using the all-sky method and VVP method, respectively. The [value values](#) of the mean winds, vorticity, divergence, and their uncertainties are also labelled.

Figure 9 shows the temporal evolution of the wind field at 88 km from 1700 UTC on 16 October 2021 to 0300 UTC on 17 October 2021 for 10 hours, at 2-hour intervals. The blue arrows represent the wind vector of the grid cell separated by 30×30 km. The red and green arrows are the winds retrieved by the all-sky method and the VVP method, respectively. The mean winds rotate clockwise with time, revealing tidal characteristics. As shown in Figure 9, when the wind field is nearly homogeneous, such as 2100 UTC on 16 October 2021, the derived wind fields are almost identical to the mean winds. [And even](#) when the wind field shows an obvious vortex structure, the derived regional wind fields and the averaged winds are well matched.



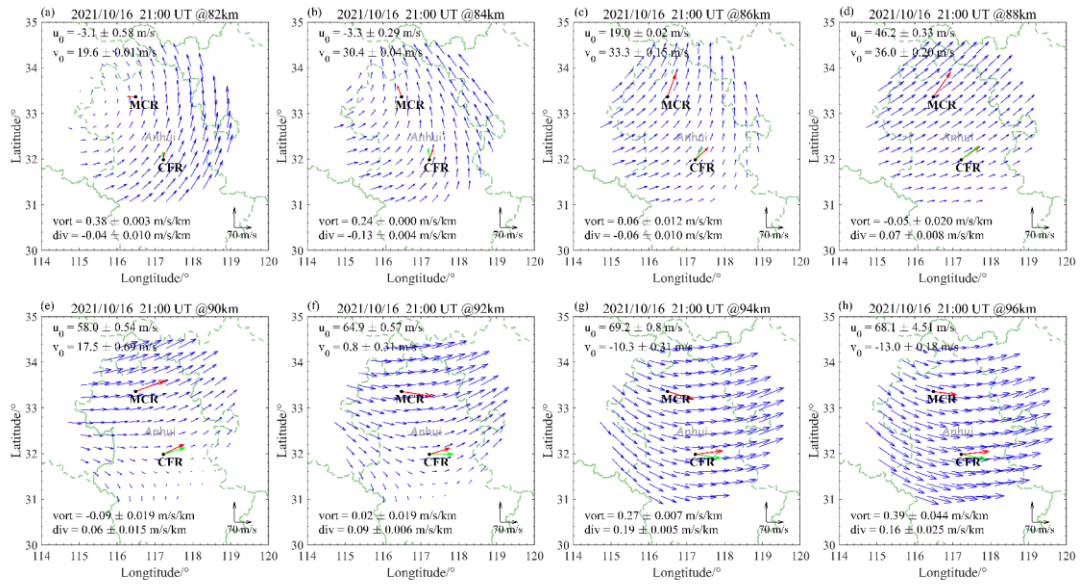


**Figure 10.** Hourly wind fields for different heights (82, 84, 86, 88, 90, 92, 94 and 96 km) at the same time (1900 UTC on 17 October 2021). The meaning of the symbols is the same as in Figure 9. The value values of the mean winds, vorticity, divergence, and their uncertainties are also labelled.

Figure 10 presents the height evolution of the wind field at 2100 UTC on 16 October 2021. The winds show distinct vortex structures at 82 and 84 km, and become more homogeneous at higher altitudes. Comparing the all-sky mean winds (red arrows) with the VVP regional winds (blue arrows) carefully, we can find that the wind magnitudes and directions are in excellent agreement, even when there are strong vortex structures. Looking at the regional winds in order of height, the characteristics of the wind changes isare similar to the temporal evolution of the wind fields, which is also a change ofin phase. The phase variation characteristics of the wind fields in height corroboratescorroborate the diurnal structure in  $u_z$  and  $v_z$ .—

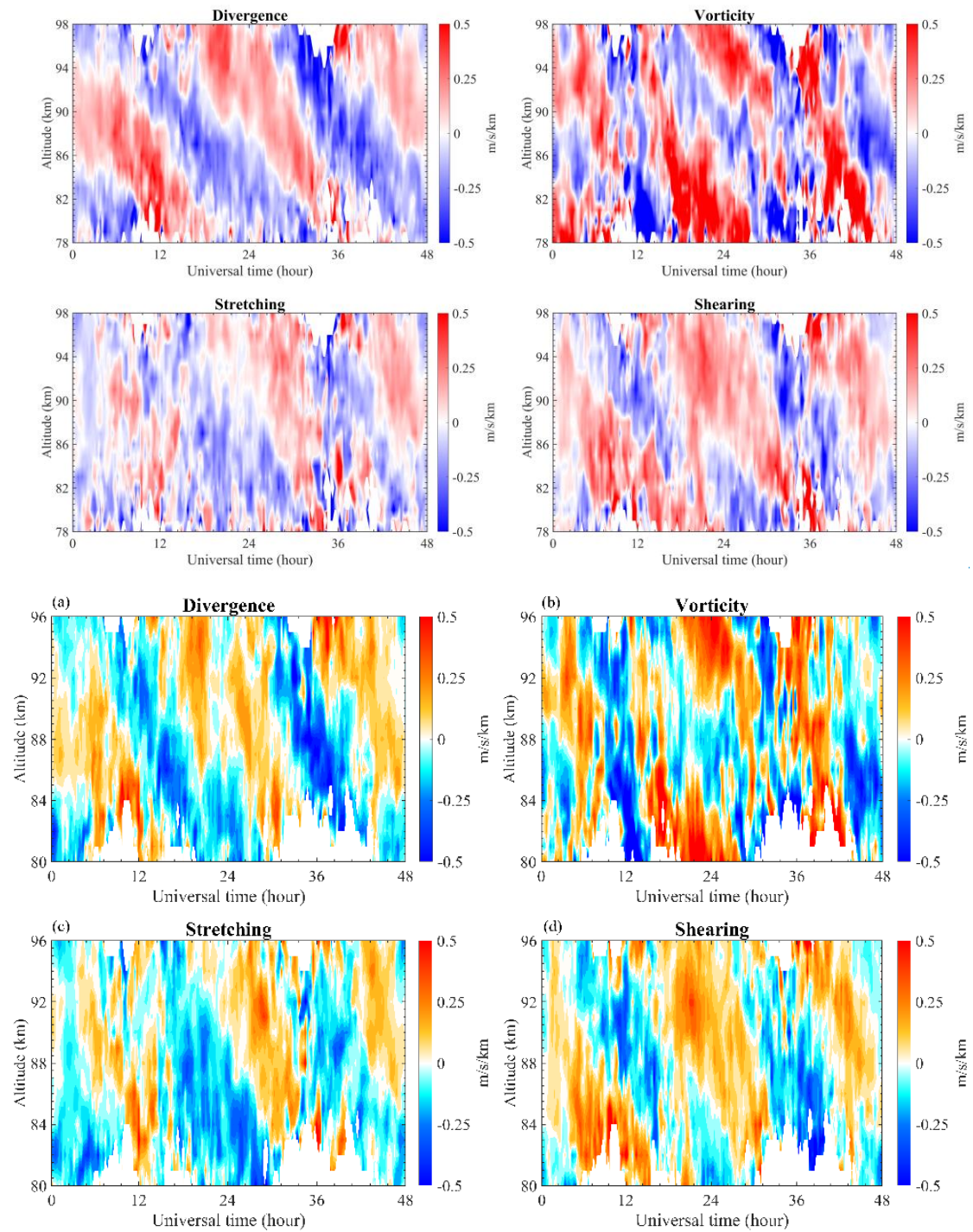


**Figure 11.** The horizontal divergence (upper left), relative vorticity (upper right), stretching deformation (lower left) and shearing deformation (lower right) calculated from the horizontal gradients of the horizontal wind [from October 16 to 17, 2021](#).

~~In order to~~ [To better](#) appreciate ~~better~~ the horizontal wind parameters, we calculate the horizontal divergence, relative vorticity, stretching deformation and shearing deformation using the horizontal gradients of the horizontal wind. As shown in ~~the~~

Figure 11, the horizontal divergence shows dominant diurnal variations with a clear upward propagating phase. The diurnal variation structure is similar to the zonal wind shown in Figure 6. Qualitatively, the zonal eastward/westward winds may correspond to the positive/negative horizontal divergence values. The relative vorticity shows more complicated vertical structures compared to the horizontal divergence. The relative vorticity mainly shows ~~the~~ semidiurnal/diurnal variations above/below 84 km. The shearing deformation is associated with the reversal of the winds, and ~~also~~ shows diurnal ~~feature~~ features. The characteristics of the stretching deformation ~~is~~ are similar to ~~that~~ those of the shearing deformation. However, the inherent relationship between the horizontal wind parameters and dynamics in the MLT region ~~is~~ still ~~not clear~~ and needs further ~~explorations.~~ exploration.

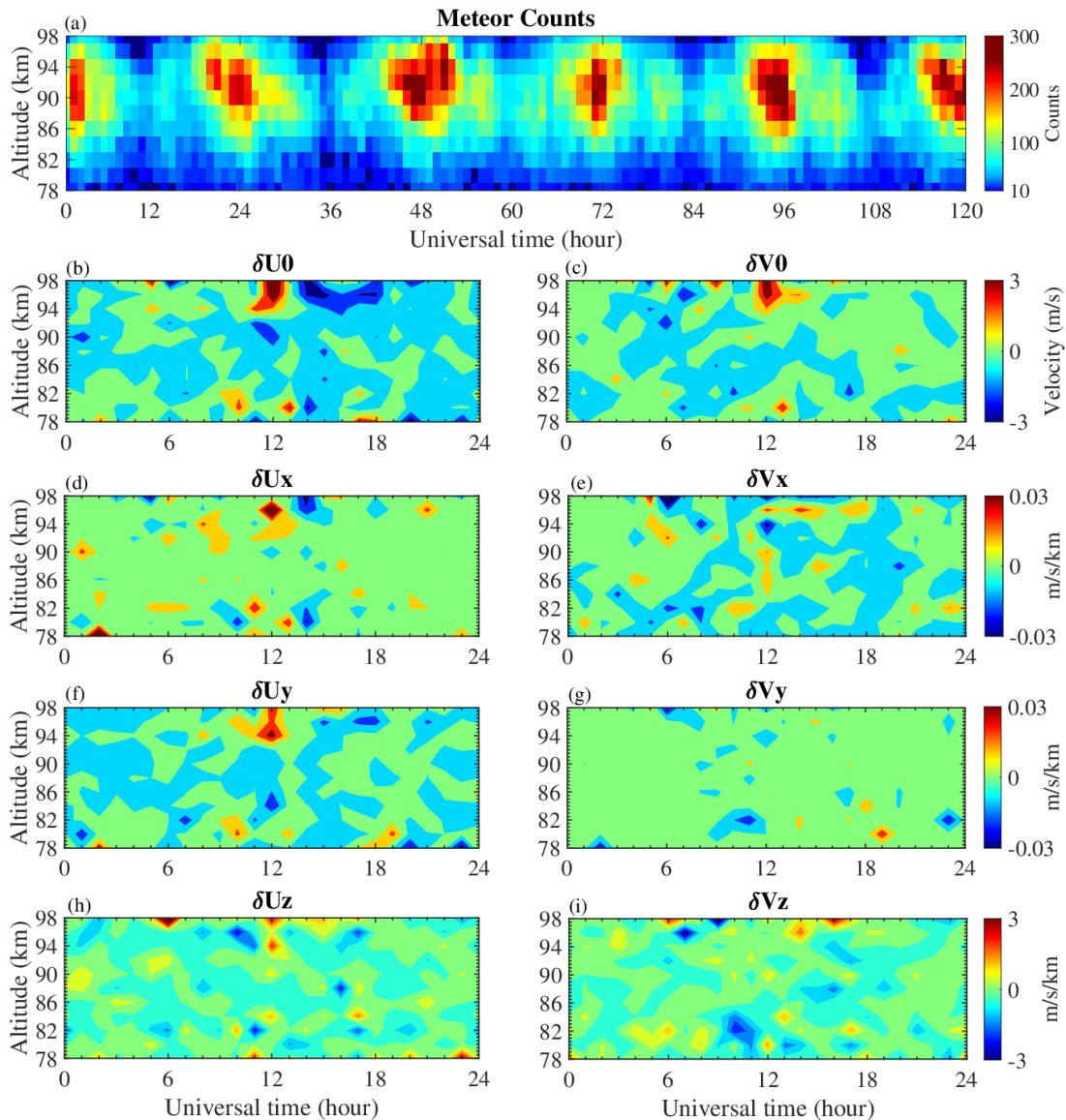




**Figure 12.** (a) ~~The valid~~Valid meteor counts ~~on~~from October 16 to ~~October~~-20, 2021. (b-i) The errors of horizontal winds and gradient terms corresponding to a composite day (October 16 to ~~October~~-20, 2021).

We stated that at least 10 meteors would be needed for estimations, and ~~actually~~ there are actually more meteor echoes involved in the calculation, which is shown in Figure 12. The valid meteor count is the number of meteors actually used in the last calculation process after several iterations. It is clear that the valid meteor counts are larger than 10 in [~~78km, 98km~~78 km, 98 km], and ~~the~~ errors due to the lack of meteor detections may be deduced. As shown in Figure 12, we estimate the errors in winds and gradient terms using the radial velocity error estimation obtained by the radar system (Holdsworth et al., 2004). The composite error estimations are shown in Figure 12 (lower four rows) ~~utilize~~utilizing the data from October 16 to October 20, 2021. It is clear that the errors of horizontal winds and gradient terms are smaller than ~~1~~1 m/s and 0.1 m/s/km, respectively, when the meteor detections are sufficient, such as the results ranging from 82 to 94 km during local morning (2000-0004 UT). The large errors basically occur above 94 km during local night (near 1200 UT), which is mainly caused by a low number of meteors.——

Our results verify the ability of ~~VVP~~the VPP method to estimate ~~the~~ wind parameters. ~~And based~~Based on these parameters, multistatic meteor radars are capable of deducing the inhomogeneities and kinetic characteristics of the wind fields, which are similar to those of Stober and Chau (2015). The increased meteor detections can reduce the error of the estimated terms and guarantee the reliability of the results. ~~Subsequent work focusing on these specific dynamics will be reported in the future.~~

##### **5. Seasonal variations dynamics parameters in MLT region**

This section uses the methodology described in the previous section to estimate the seasonal variation in MLT dynamics parameters, including horizontal wind deformations and gravity wave (GW) momentum fluxes, in the MLT region in the middle latitudes of the Northern Hemisphere from February 2022 to February 2023. As shown in Figure 13, we present the seasonal variations in monthly mean horizontal winds, horizontal divergence, relative vorticity, stretching deformation, and shearing

deformation. In Figure 13a, the zonal component shows westward winds in spring (March, April and May) and eastward winds in summer, autumn and winter (May to February) below 84 km, which is the characteristic of annual variation. However, within 84 to 90 km, the zonal wind shows maxima value in summer and winter as well as minimum value at the spring and autumn equinox, suggesting semiannual variation. From 90 to 96 km, the zonal wind again shows annual variation, with large eastward winds in spring to summer and low westward winds in autumn to winter. The overall zonal wind between 80 and 96 km is characterized by annual variation. During spring to summer, the zonal wind increases (greater eastward and lesser westward) with altitude, reaching a peak value of approximately 50 m/s at 96 km in May. In autumn and winter, the zonal wind decreases (lesser eastward and greater westward) with altitude, reaching a minimum value at 96 km in November.

In Figure 13b, the meridional winds show similar structures to the zonal winds. Below 86 km, the meridional wind is southward in spring to summer and northward in autumn to winter. Meanwhile, at latitudes between 88 and 96 km, the meridional wind is northward in spring to summer and is northward in autumn to winter, and the maximum values of northward and southward winds are 20 m/s and 15 m/s in May and October, respectively.

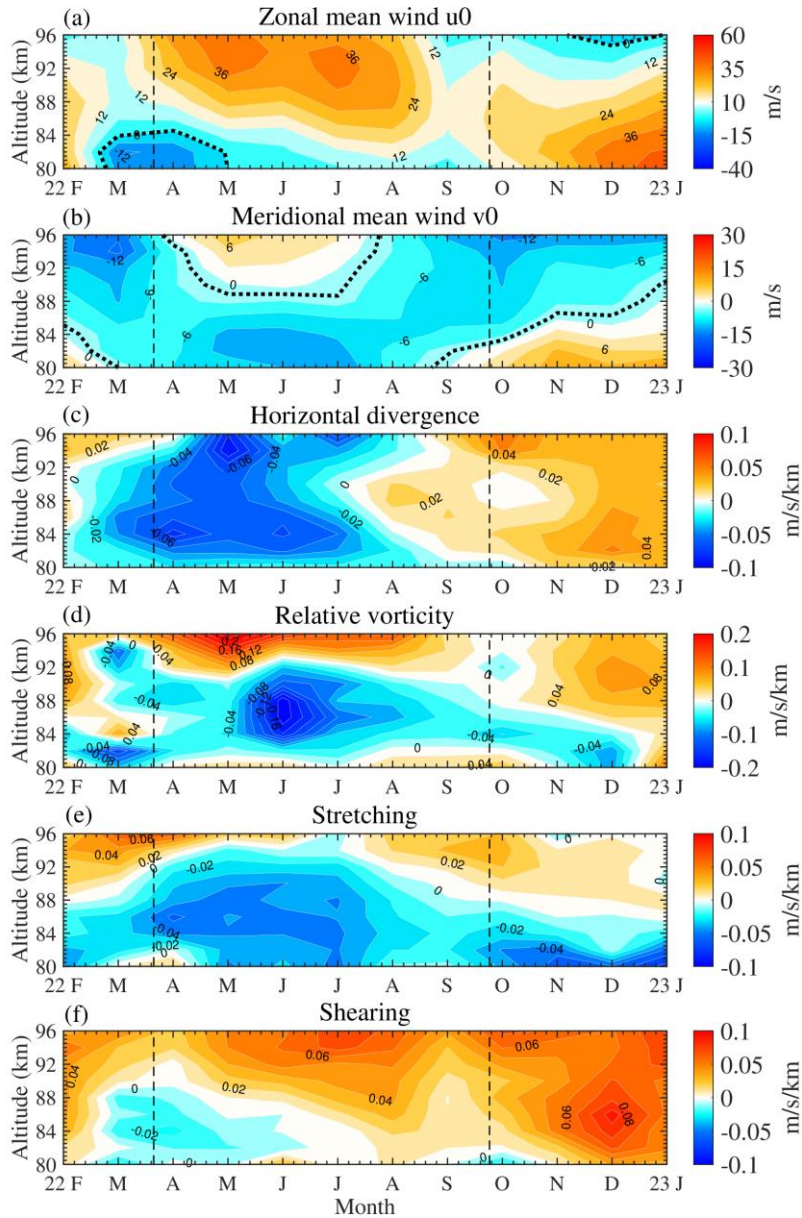


**Figure 13.** The seasonal values of horizontal winds and wind deformations from February 1, 2022 to February 1, 2023 at altitudes ranging from 80 to 96 km: (a) mean zonal wind, (b) mean meridional wind, (c) horizontal divergence, (d) relative vorticity, (e) stretching deformation, and (f) shearing deformation.

In Figures 13c and 13d, the horizontal divergence and stretching deformation are calculated by the gradient terms  $u_x$  and  $v_y$ , and they portray a similar seasonal variation. The divergence is almost negative below 84 km. Within 84 to 96 km, the value is still negative in March to June, reaching -0.1 m/s/km at 96 km in May. In the remaining months of the year, the divergence is positive, reaching 0.08 m/s/km at 94 km in November. The maximum values of divergence (convergence) correspond to the

maxima of eastward/northward (westward/southward) wind velocities. For the stretching deformation, the result is totally negative below 88 km and shows the most negative value of -0.08 m/s/km at 80 km in January. In the upper altitude, the results are nearly negative in April to August and nearly positive in September to February, reaching 0.05 m/s/km at 96 km in February, which also corresponds to the maxima of the horizontal winds.

The relative vorticity in Figure 13e shows a clear stratification with height in summer and autumn, which is similar to the polar results reported by Chau et al. (2017). The value is negative between 84 and 92 km, with a maximum of -0.08 m/s/km in August at 88 km, and is positive below or above this height range. The maximum positive value is 0.18 m/s/km in January at 96 km. Finally, the wind shearing deformation, as shown in Figure 13e, is close to 0 and even negative near the spring and autumn equinox, which corresponds exactly to the annual variation structure of the background mean winds. The minimum and maximum values are both at 88 km, -0.04 m/s/km and 0.09 m/s/km, respectively, in March and December.

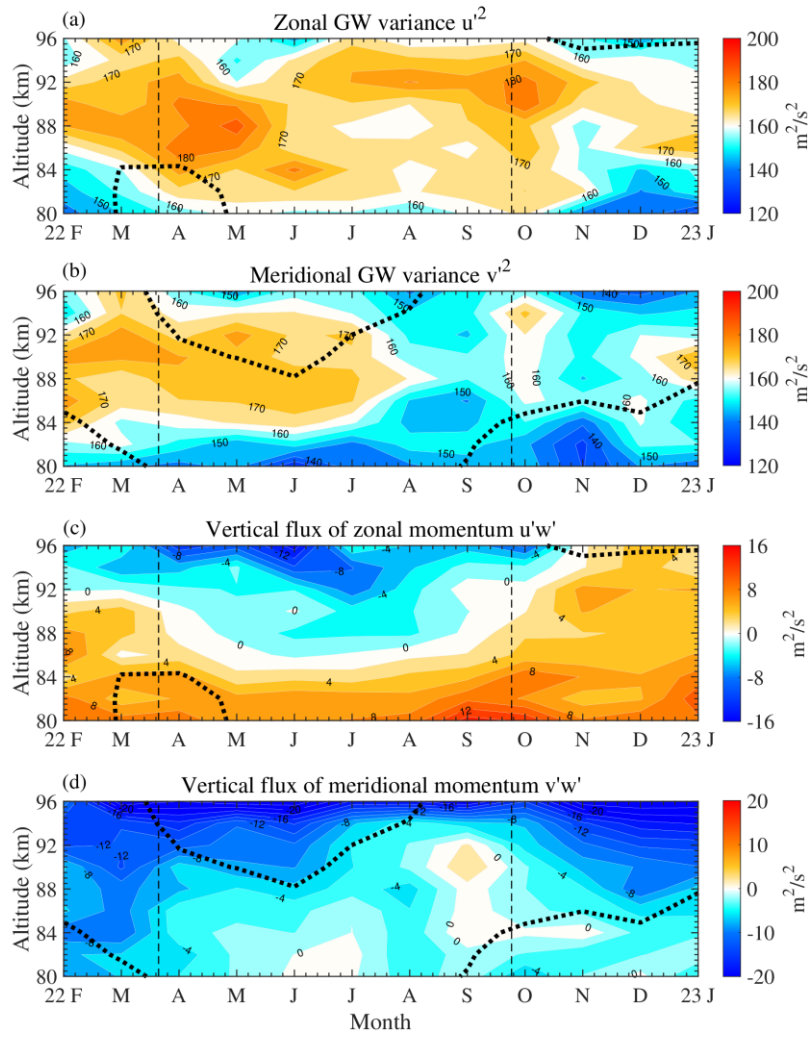


**Figure 14.** Height-time cross-sections of the zonal (a) and meridional (b) wind variance and the vertical flux of zonal (c) and meridional (d) momentum. Running averages over 30 days shifted by 7 days from February 2022 to February 2023. The black dashed lines indicate the zero mean zonal wind in (a) and (c) and zero mean meridional wind in (b) and (d).

Compared to monostatic meteor radar, more meteor detections and different viewing angles of the radial velocity observed by the bistatic meteor radar system can appreciably improve the precision of the GW covariance estimation (Spargo et al., 2019). In addition, we also try to use the bistatic meteor radar system to estimate the GW momentum fluxes, basically following the method introduced by Hocking (2005), Jia et al. (2018), Spargo et al. (2019) and the references therein. Figure 14 presents the seasonal variations in GW momentum flux terms.

As shown in Figures 14a and 14b, the zonal ( $u'^2$ ) and meridional ( $v'^2$ ) GW variance terms generally increase with height below ~90 km and then decrease with height above 90 km, reflecting the characteristics of the GW amplitude variation. The zonal GW variances indicate a semiannual variation, with two maxima around April and October and two minima in August and December.

The meridional ( $v'^2$ ) GW variance mainly shows annual variation, with a maximum amplitude in winter and spring and a minimum amplitude in summer and autumn. Below 90 km, most gravity waves are unsaturated, so the amplitude of the gravity wave increases exponentially due to the decreasing air density, thus causing the GW variance to increase with height. Up to approximately 90 km, when the gravity wave is saturated, according to linear theory, the gravity wave will become unstable and break, leading to a decrease in the GW variance (Fritts, 1984; Placke et al., 2011).

In Figures 14c and 14d, the vertical fluxes of zonal ( $v'w'$ ) and meridional ( $u'w'$ ) momentum basically show a U-shape and an inverted U-shape, respectively. Both  $u'w'$  and  $v'w'$  decrease with height throughout the year, except for  $v'w'$  in September, when both reach maxima in September and minima in June but at different corresponding altitudes. Moreover, the meridional component appears to be southward during almost the whole year. These results are generally comparable with those of a previous study observed by Wuhan (30.2°N, 114.2°E) and Beijing (40°N, 116.3°E) at middle latitudes (e.g., Jia et al., 2018). Placke et al. (2011) reported that the GW activity in the upper mesosphere over Collm, Germany (51.31°N, 13.01°E) at higher-middle latitudes has a semiannual oscillation with the main maximum in summer and a minor maximum in winter. Combined with the background wind structure, we can see the influence of gravity waves on the structure of the background mean winds. From May to August, it can be considered that only the westward gravity wave can propagate upward under the background of the prevailing eastward wind, and the meanwhile, the westward momentum flux will produce the northward drag force under the action of the Coriolis force and thus slow down the southward wind.

## **6. Discussion and Summary**

In this study, we have presented ~~the~~ preliminary results from the Mengcheng and

Changfeng bistatic meteor radar systems. The main objectives were accomplished successfully by the new bistatic meteor radar system and are summarized as follows:

1. The bistatic meteor radar system consists of a conventional meteor radar located at Mengcheng and a remote receiver located at Changfeng. The remote receiver observes the forward scatter meteor echoes transmitted from the Mengcheng transmitter. Compared to the monostatic meteor radar operation, we detect ~70% more forward scatter meteor detections by using the bistatic radar system. In addition, the forward scatter meteor echoes provide different viewing angles of the radial velocity and a larger viewing area of the atmosphere compared to the monostatic backscatter meteor radar.
2. Based on a distance of 167.3 km between the radar transmitter and remote receiver, those quantities depending on the geometry of the forward scatter arrangement, such as the forward scatter angle, equivalent frequencies and Bragg wavelength, were estimated. The forward scatter meteor echoes are normally ~1 km higher than the backscatter meteor echoes because the equivalent frequencies (the effective Bragg wavelengths) of forward scattering are lower (larger) than those of backscatter meteor echoes (Cepelcha et al., 1998). The bistatic meteor radar system generally provides a more than 400 km×400 km horizontal viewing area.
3. Taking advantage of the increased meteor number and different viewing angles observed by the bistatic meteor radar system, we can relax the assumption of a homogeneous horizontal wind and estimate the two-dimensional horizontal wind more accurately using the volume velocity processing method. The improved wind estimation provides the mean winds and the inhomogeneities of the winds (such as the horizontal divergence, relative horizontal vorticity, stretching and shearing deformation). [In addition, the seasonal variation of atmospheric dynamics parameters, including horizontal wind deformations and gravity wave \(GW\) momentum fluxes, in the MLT region at middle latitudes of the Northern Hemisphere are presented.](#)

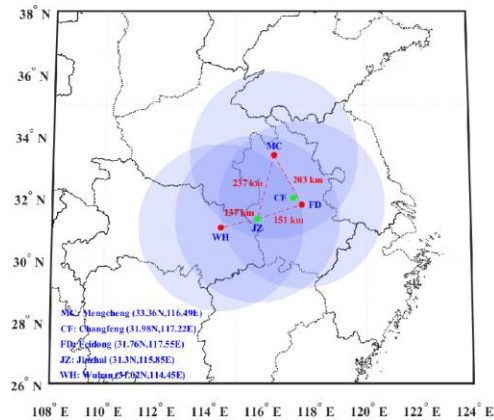


**Figure 4.15.** Design schematic view of the multistatic meteor radar network. The red dots represent the monostatic meteor radars located in Mengcheng, Feidong and Wuhan. The green dots represent the remote receivers at Changfeng and Jinzhai. The distance between each site is marked. The blue shaded areas label a circle of 300 km in diameter around each centre of the radial velocity measurements.

The preliminary results of the MLT region observed by our bistatic meteor radar system are encouraging, and lay a foundation for an extension of the new multistatic meteor radar network. Figure 4.15 shows the design schematic view of the new multistatic meteor radar system in Central-Eastern China. At present, we are installing a new monostatic meteor radar at Feidong (31.76°N, 117.55°E). The distance between the Feidong and Mengcheng meteor radars is approximately 203 km, which will enable transmitting and receiving for Mengcheng and Feidong meteor radars from each other. Then, the Changfeng remote receiver will be moved to Jinzhai, and the Jinzhai site will be able to receive the forward scatter meteor echoes from the Mengcheng, Feidong and Wuhan (e.g., Zhou et al., 2022) meteor radars, which all operate at 38.9 MHz. The new multistatic meteor radar system will achieve three backscatter (monostatic) links and five forward scatter (bistatic) links, which would provide us with 6 times more meteor detections than a conventional (monostatic) meteor radar.

The new multistatic meteor radar network will provide a better determination of the horizontal and vertical gradients of the horizontal winds by increasing the meteor



number and extending the atmospheric viewing area, which allows us to investigate gravity waves with horizontal scales smaller than hundreds of kilometers (e.g., Stober et al., 2018, 2021b, 2022; Conte et al., 2020; [Poblet et al., 2022](#)) and estimate a higher temporal resolution of the standard horizontal mean wind (e.g., Vierinen et al., 2019; Vargas et al., 2021; Zhong et al., 2021). Moreover, the multistatic meteor radar network can estimate not only the mean horizontal and vertical winds but [also](#) additional quantities, such as the horizontal divergence, relative vorticity, stretching, and shearing deformation of the wind field (e.g., Stober et al., 2015; Chau et al., 2017, 2020; Volz et al., 2021). In addition, multistatic meteor radar data can also be used to investigate smaller-scale MLT perturbations by estimating the second-order statistics of radial velocities, for example, the gravity wave momentum fluxes in the MLT region (e.g., Spargo et al., 2019). Furthermore, the decay time or ambipolar diffusion coefficient of meteor trails measured by multistatic meteor radar can be used to estimate the mesospheric neutral temperature, pressure and density (e.g., Hocking et al., 1997; 1999; Younger et al., 2015; Yi et al., 2019; [2021](#)), as well as the mesospheric ozone density (Sukara, 2013). The velocity and spatial position information of meteors can be used for meteor orbit and meteor shower detection (e.g., Holdsworth et al., 2007; Younger et al., 2015). We are confident that the multistatic meteor radar network system is a powerful technique for achieving comprehensive observation of the MLT region and will provide an opportunity to understand MLT dynamics.

***Author contributions.*** WY and XX designed the study. WY and JZ carried out the data analysis and wrote the paper. XX supervised the work and provided valuable comments. IMR revised the paper. All of the authors discussed the results and commented on the paper.

***Acknowledgments:*** Wen Yi acknowledge the technical support of our radar systems by Chris Adami and Jinsong Chen. We would like to thank Gunter Stober and Zishun Qiao for useful discussions regarding this work.

***Financial support.***

*This work was supported by* the National Natural Science Foundation of China (grants No. 42174183, 42125402, 41974174, 42188101 and 41831071), the B-type Strategic

Priority Program of CAS (grant No. XDB41000000), the Project of Stable Support for Youth Team in Basic Research Field, CAS (grant No. YSBR-018), the Fundamental Research Funds for the Central Universities (grant No. YD3420002004), the Joint Open Fund of Mengcheng National Geophysical Observatory (MENGO-202209), the Anhui Provincial Natural Science Foundation (grant no. 2008085MD113), the Open Research Project of Large Research Infrastructures of CAS - “Study on the interaction between low/mid-latitude atmosphere and ionosphere based on the Chinese Meridian Project.

**Data Availability Statement:** The data presented in this study are available on request from the author (Y.W., yiwen@ustc.edu.cn). The data are not publicly available due to institutional restrictions.

**Conflicts of Interest:** The authors declare no conflict of interest.

## Reference

- Andrioli V F, Fritts D C, Batista P P, and Clemesha B R. 2013. Improved analysis of all-sky meteor radar measurements of gravity wave variances and momentum fluxes, *Ann. Geophys.*, 31, 889–908, <https://doi.org/10.5194/angeo-31-889-2013>
- Aso T, Tsuda T, Kato S. 1979. Meteor radar observations at Kyoto University'. *Journal of Atmospheric and Terrestrial Physics*, 41, 517-525.
- Avery S K, Riddle A C, Balsley B B. 1983. The Poker Flat, Alaska, MST radar as a meteor radar, *Radio Sci.*, 18(6), 1021– 1027.
- Browning K A, Wexler R. 1968. The Determination of Kinematic Properties of a Wind Field Using Doppler Radar, *Journal of Applied Meteorology*, 7, 105-113, doi:10.1175/1520-0450(1968)007<0105:Tdokpo>2.0.Co;2.
- Cepelcha Z, Borovička J Í, Elford W G, ReVelle D O, Hawkes R L, Porubčan V Í, Šimek M. 1998. Meteor phenomena and bodies. *Space Science Reviews*, 84(3/4), 327–471. <https://doi.org/10.1023/A:1005069928850>
- Cervera MA, Reid I M. 1995. Comparison of simultaneous wind measurements using colocated VHF meteor radar and MF spaced antenna radar systems, *Radio Science*, 30(4), 1245-1261, doi:10.1029/95rs00644.
- Chau J L, Stober G, Hall C M, Tsutsumi M, Laskar F I, Hoffmann P. 2017. Polar mesospheric horizontal divergence and relative vorticity measurements using multiple specular meteor radars. *Radio Science*, 52, 811–828. <https://doi.org/10.1002/2016RS006225>
- Chau J L, Urco J M, Vierinen J, Harding B J, Clahsen M, Pfeffer N, et al. 2021. Multistatic specular meteor radar network in Peru: System description and initial results. *Earth and Space Science*, 8, e2020EA001293. <https://doi.org/10.1029/2020EA001293>
- Conte J F, Chau J L, Urco J M, Latteck R, Vierinen J, Salvador J O. 2021. First studies of mesosphere and lower thermosphere dynamics using a multistatic specular

- meteor radar network over southern Patagonia. *Earth and Space Science*, 8, e2020EA001356. <https://doi.org/10.1029/2020EA001356>
- de Elía R, Zawadzki I. 2001. Optimal layout of a bistatic radar network, *J. Atmos. Oceanic Technol.*, 18, 1184–1194.
- Doviak R J, Zrnic D S. 2006. *Doppler Radar and Weather Observations*, 2nd ed., Dover, Mineola.
- Elford W G. 1959. A study of winds between 80 and 100 km in medium latitudes, *Planet. Space Sci.*, 1, 94–101
- Elford W G, Robertson D S. 1953. Measurements of winds in the upper atmosphere by means of drifting meteor trails II'. *Journal of Atmospheric and Terrestrial Physics*, 4, 271-284.
- Forbes J M, Garrett H B. 1979. Theoretical studies of atmospheric tides. *Reviews of Geophysics and Space Physics*, 17(8), 1951–1981. <https://doi.org/10.1029/RG017i008p01951>
- [Fritts, D. C.: Gravity wave saturation in the middle atmosphere: A review of theory and observations, \*Reviews of Geophysics.\*, 22, 275–308, 1984.](#)
- Fritts D C, Alexander M J. 2003. Gravity wave dynamics and effects in the middle atmosphere. *Reviews of Geophysics*, 41(1), 1003. <https://doi.org/10.1029/2001RG000106>
- Fritts D C, et al. 2010. Southern Argentina Agile Meteor Radar: System design and initial measurements of large-scale winds and tides, *J. Geophys. Res.*, 115, D18112, doi:10.1029/2010JD013850.
- Fritts D C, Janches D, Hocking W K, Mitchell, N J, Taylor M J. 2012. Assessment of gravity wave momentum flux measurement capabilities by meteor radars having different transmitter power and antenna configurations. *Journal of Geophysical Research*, 117, D10108. <https://doi.org/10.1029/2011JD017174>
- Hocking W K, Thayaparan T, Jones J. 1997. Meteor decay times and their use in determining a diagnostic mesospheric temperature-pressure parameter: Methodology and one year of data, *Geophys. Res. Lett.*, 24, 2977–2980, doi:10.1029/97GL03048.
- Hocking W K, 1999. Temperatures using radar-meteor decay times, *Geophys. Res. Lett.*, 26, 3297–3300, doi:10.1029/1999GL003618.
- Hocking W K, Fuller B, Vandepier B. 2001. Real-time determination of meteor-related parameters utilizing modern digital technology. *Journal of Atmospheric and Solar-Terrestrial Physics*, 63(2), 155–169.
- Hocking W K. 2005. A new approach to momentum flux determinations using SKiYMET meteor radars. *Annales Geophysicae*, 23(7), 2433–2439.
- Holdsworth D A, Reid I M, Cervera M A. 2004. Buckland Park all-sky interferometric meteor radar. *Radio Science*, 39, RS5009. <https://doi.org/10.1029/2003RS003014>
- Holdsworth D A, Elford W G, Vincent R A, Reid I M, Murphy D J, Singer W. 2007. All-sky interferometric meteor radar meteoroid speed estimation using the fresnel transform. *Ann. Geophys.*, 25, 385–398.
- Jia M, Xue X., Gu S, Chen T, Ning B, Wu J, et al. 2018. Multiyear observations of gravity wave momentum fluxes in the midlatitude mesosphere and lower

- thermosphere region by meteor radar. *Journal of Geophysical Research: Space Physics*, 123. <https://doi.org/10.1029/2018JA025285>
- Jones J, Webster A R, Hocking W K. 1998. An improved interferometer design for use with meteor radars, *Radio Science*, 33(1), 55-65, doi:10.1029/97rs03050.
- Manson A H, Meek C, Hagan M, Koshyk J, Franke S, Fritts D, Hall C, Hocking W, Igarashi K, MacDougall J, Rigglin D, Vincent R. 2002. Seasonal variations of the semi-diurnal and diurnal tides in the MLT: multi-year MF radar observations from 2-70N, modelled tides (GSWM, CMAM). *Ann. Geophys.*, 20, 661-677.
- Nicolls M J, Fritts D C, Janches D, Heinselman C J. 2012. Momentum flux determination using the multi-beam Poker Flat Incoherent Scatter Radar, *Ann. Geophys.*, 30, 945–962, <https://doi.org/10.5194/angeo-30-945-2012>
- [Placke, M., Stober, G., and Jacobi, C.: Gravity wave momentum fluxes in the MLT– Part I: seasonal variation at Collm \(51.3° N, 13.0° E\), \*J. Atmos. Sol.-Terr. Phys.\*, 73, 904–910, 2011.](#)
- [Poblet, F. L., Chau, J. L., Conte, J. F., Avsarkisov, V., Vierinen, J., & Charuvil Asokan, H. \(2022\). Horizontal wavenumber spectra of vertical vorticity and horizontal divergence of mesoscale dynamics in the mesosphere and lower thermosphere using multistatic specular meteor radar observations. \*Earth and Space Science\*, 9, e2021EA002201. <https://doi.org/10.1029/2021EA002201>.](#)
- Reid I M, Rüster R, Czechowsky P, Schmidt G. (1988). VHF radar measurements of momentum flux in the summer polar mesosphere over Andenes (69°N, 16°E), Norway, *Geophys. Res. Lett*, 15, 1263–1266
- Reid, I. M. (2015). MF and HF radar techniques for investigating the dynamics and structure of the 50 to 110 km height region: A review. *Progress in Earth and Planetary Science*, 2, 33. <https://doi.org/10.1186/s40645-015-0060-7>
- Reid I M, Younger J. (2016). 65 years of meteor radar research at Adelaide, Conference Proceedings of the International Meteor Conference Egmond, the Netherlands, 242-246, 2016, <http://adsabs.harvard.edu/abs/2016pimo.conf..242R>
- Robertson D S, Liddy D T, Elford W G. 1953. Measurements of winds in the upper atmosphere by means of drifting meteor trails I. *Journal of Atmospheric and Terrestrial Physics*, 4(4), 255-270.
- Roper R G, Elford W G. 1963. Seasonal variation of turbulence in the upper atmosphere, *Nature*, 197, 963–964
- Roper R G. 1966. Atmospheric turbulence in the meteor region, *J. Geophys. Res.*, 71(24), 5785–5792.
- Roper R G. 1975. The measurement of meteor winds over Atlanta (34° N, 84° W), *Radio Sci.*, 10(3), 363–369, doi:10.1029/RS010i003p00363.
- Salby M L. 1984. Survey of planetary-scale traveling waves: The state of theory and observations, *Rev. Geophys.*, 22(2), 209–236, doi:10.1029/RG022i002p00209.
- Spargo A J, Reid I M, MacKinnon A D. 2019. Multistatic meteor radar observations of gravity-wave tidal interaction over southern Australia. *Atmospheric Measurement Techniques*, 12(9), 4791–4812. <https://doi.org/10.5194/amt-12-4791-2019>
- Stober G, Sommer S, Rapp M, Latteck R. 2013. Investigation of gravity waves using horizontally resolved radial velocity measurements. *Atmos. Meas. Tech.*, 6, 2893-

2905.

- Stober G, Chau J. (2015). A multistatic and multifrequency novel approach for specular meteor radars to improve wind measurements in the MLT region. *Radio Science*, 50, 431–442. <https://doi.org/10.1002/2014rs005591>
- Stober G, Chau J L, Vierinen J, Jacobi C, Wilhelm S. 2018. Retrieving horizontally resolved wind fields using multi-static meteor radar observations. *Atmos. Meas. Tech.*, 11(8), 4891–4907.
- Stober G, Baumgarten K, McCormack J P, Brown P, Czarnecki J. (2020). Comparative study between ground-based observations and NAVGEM-HA analysis data in the mesosphere and lower thermosphere region. *Atmos. Chem. Phys.*, 20(20), 11979–12010. doi:10.5194/acp-20-11979-2020
- Stober, G., Kuchar, A., Pokhotelov, D., Liu, H., Liu, H.-L., Schmidt, H., Jacobi, C., Baumgarten, K., Brown, P., Janches, D., Murphy, D., Kozlovsky, A., Lester, M., Belova, E., Kero, J., and Mitchell, N. (2021a) Interhemispheric differences of mesosphere–lower thermosphere winds and tides investigated from three whole-atmosphere models and meteor radar observations, *Atmos. Chem. Phys.*, 21, 13855–13902, <https://doi.org/10.5194/acp-21-13855-2021>
- Stober G, Kozlovsky A, Liu A, Qiao Z, Tsutsumi M, Hall C, Nozawa S, Lester M, Belova E, Kero J, Espy P J, Hibbins R E, Mitchell N. (2021b). Atmospheric tomography using the Nordic Meteor Radar Cluster and Chilean Observation Network De Meteor Radars: network details and 3D-Var retrieval, *Atmos. Meas. Tech.*, 14, 6509–6532, <https://doi.org/10.5194/amt-14-6509-2021>
- Stober, G., Liu, A., Kozlovsky, A., Qiao, Z., Kuchar, A., Jacobi, C., Meek, C., Janches, D., Liu, G., Tsutsumi, M., Gulbrandsen, N., Nozawa, S., Lester, M., Belova, E., Kero, J., and Mitchell, N. (2022) Meteor radar vertical wind observation biases and mathematical debiasing strategies including the 3DVAR+DIV algorithm, *Atmos. Meas. Tech.*, 15, 5769–5792, <https://doi.org/10.5194/amt-15-5769-2022>.
- Sukara R E. 2013. Potential for measurement of mesospheric ozone density from overdense meteor trains with a monostatic meteor radar, electronic thesis and dissertation repository, Pap. 1789, Univ. of Western Ontario, Canada
- Vierinen J, Chau J L, Charuvil H, Urco J M, Clahsen M, Avsarkisov V. et al. 2019. Observing mesospheric turbulence with specular meteor radars: A novel method for estimating second-order statistics of wind velocity. *Earth and Space Science*, 6, 1171–1195. <https://doi.org/10.1029/2019EA000570>
- Vincent R A, Reid I M. 1983. HF Doppler measurements of mesospheric gravity wave momentum fluxes. *Journal of the Atmospheric Sciences*, 40(5), 1321–1333.
- Vincent R A. 2015. The dynamics of the mesosphere and lower thermosphere: a brief review, *Progress in Earth and Planetary Science*, 2(1), doi:10.1186/s40645-015-0035-8.
- Vincent R A, Kovalam S, Reid I M, Younger J P. 2010. Gravity wave flux retrievals using meteor radars. *Geophysical Research Letters*, 37. <https://doi.org/10.1029/2010GL044086>
- Volz R, Chau J L, Erickson P J, Vierinen J P, Urco J M, Clahsen M. 2021, Four-dimensional mesospheric and lower thermospheric wind fields using Gaussian

- process regression on multistatic specular meteor radar observations, *Atmos. Meas. Tech.*, 14, 7199–7219, <https://doi.org/10.5194/amt-14-7199-2021>
- Waldteufel P, Corbin H. 1979. ANALYSIS OF SINGLE-DOPPLER RADAR DATA, *Journal of Applied Meteorology*, 18(4), 532-542, doi:10.1175/1520-0450(1979)018<0532:Otaosd>2.0.Co;2.
- Xiong J, Wan W, Ning B, Liu L. 2004. First results of the tidal structure in the MLT revealed by Wuhan Meteor Radar (30°40'N, 114°30'E), *J. Atmos. Sol. Terr. Phys.*, 66(6–9), 675–682.
- Yi, W., Xue, X., Chen, J., Dou, X., Chen, T., and Li, N.: Estimation of mesopause temperatures at low latitudes using the Kunming meteor radar, *Radio Sci.*, 51, 130–141, <https://doi.org/10.1002/2015RS005722>, 2016.
- Yi W, Xue X, Reid I M, Younger J P, Chen J, Chen T, Li N. 2018. Estimation of mesospheric densities at low latitudes using the Kunming meteor radar together with SABER temperatures. *Journal of Geophysical Research: Space Physics*, 123. <https://doi.org/10.1002/2017JA025059>
- Yi W, Xue X, Reid I M, Murphy D J, Hall C M, Tsutsumi M, Ning B, Li, G., Vincent, R. A., Chen, J., Wu, J., Chen, T., and Dou, X. (2019). Climatology of the mesopause relative density using a global distribution of meteor radars, *Atmospheric Chemistry and Physics*, 19, 7567-7581, <https://doi.org/10.5194/acp-19-7567-2019>.
- Yi W, Xue X, Reid I M, Murphy D J, Hall C M, Tsutsumi M, et al. 2021. Climatology of interhemispheric mesopause temperatures using the high-latitude and middle-latitude meteor radars. *Journal of Geophysical Research: Atmospheres*, 126, e2020JD034301. <https://doi.org/10.1029/2020JD034301>
- Younger J P, Reid I M, Vincent, R. A., & Murphy, D. J. (2015). A method for estimating the height of a mesospheric density level using meteor radar. *Geophys. Res. Lett.*, 42, 6106–6111, doi:10.1002/2015GL065066
- Younger, J. P., Reid, I. M., Li, G., Ning, B., & Hu, L. (2015). Observations of the new Camelopardalids meteor shower using a 38.9 MHz radar at Mohe, China. *Icarus*, 253, 25-30.
- Yu Y, Wan W, Ning B, Liu L, Wang Z, Hu L, Ren Z. 2013. Tidal wind mapping from observations of a meteor radar chain in December 2011, *J. Geophys. Res. Space Physics*, 118, 2321–2332, doi:10.1029/2012JA017976.
- Zeng, J.; Yi, W.; Xue, X.; Reid, I.; Hao, X.; Li, N.; Chen, J.; Chen, T.; Dou, X. Comparison between the Mesospheric Winds Observed by Two Collocated Meteor Radars at Low Latitudes. *Remote Sens.* 2022, 14, 2354. <https://doi.org/10.3390/rs14102354>
- Zhong W, Xue X, Yi W, Reid I M, Chen T, Dou X. 2021. Error analyses of a multistatic meteor radar system to obtain a 3-dimensional spatial resolution distribution, *Atmospheric Measurement Techniques*, <https://doi.org/10.5194/amt-2020-353>.
- Zhou X, Yue X, Yu Y, Hu L. 2022. Day-to-day variability of the MLT DE3 using joint analysis on observations from TIDI-TIMED and a meteor radar meridian chain. *Journal of Geophysical Research: Atmospheres*, 127, e2021JD035794. <https://doi.org/10.1029/2021JD035794>

